

Supporting Information

Bioengineering a Single-Protein Junction

Marta P. Ruiz^{†##§}, Albert C. Aragonès^{†##§}, Nuria Camarero[#], J. G. Vilhena^{¶Ω}, Maria Ortega[¶], Linda A. Zotti[¶], Rubén Pérez^{¶Δ}, Juan Carlos Cuevas^{¶Δ}, Pau Gorostiza^{##§*}, Ismael Díez-Pérez^{†##§*}

[†] Departament of Materials Science and Physical Chemistry & Institute of Theoretical and Computational Chemistry (IQTCUB), University of Barcelona, Martí i Franquès, 1, Barcelona 08028 Spain.

[#] Institute for Bioengineering of Catalonia (IBEC), Baldri Reixac 15-21, Barcelona 08028 Spain.

[§] Centro Investigación Biomédica en Red (CIBER-BBN). Campus Río Ebro-Edificio I+D, Poeta Mariano Esquillor s/n, 50018 Zaragoza, Spain.

[‡] Catalan Institution for Research and Advanced Studies (ICREA)

[¶] Departamento de Física Teórica de la Materia Condensada, Universidad Autónoma de Madrid, E-28049 Madrid, Spain.

^Ω Department of Macromolecular Structures, Centro Nacional de Biotecnología, Consejo Superior de Investigaciones Científicas, 28049 Cantoblanco, Madrid, Spain.

^Δ Condensed Matter Physics Center (IFIMAC), Universidad Autónoma de Madrid, E-28049 Madrid, Spain.

Table of Contents

- 1. Chemicals and material**
- 2. K41C Azurin mutant**
 - a. Design of the K41C mutant**
 - b. Expression and purification of the K41C mutant**
- 3. Spectroscopic characterization**
 - a. UV-visible spectroscopy**
 - b. Fluorescence spectroscopy**
- 4. Electrochemical characterization**
 - a. Sample preparation**
 - b. Cyclic voltammetry (CV)**
- 5. Electrochemical Scanning Tunnelling Microscopy (ECSTM)**
 - a. Sample preparation**
 - b. ECSTM measurements**
- 6. Transmission electron microscopy (TEM) of protein-functionalized Au nanoparticles**
- 7. Computational methods and details**
 - a. Visualization of the frontier orbitals and calculation of their energies for the studied protein fragment**
 - b. Molecular Dynamics Simulations**
 - c. Temperature-dependent conductance in a sequential 2-step model**

1. Chemicals and material

List of employed chemicals and materials:

Azurin from *Pseudomonas aeruginosa* (lyophilized powder), Potassium phosphate dibasic solution 1.0M, Sodium phosphate monobasic dehydrate, Potassium Cyanide, Sodium Chloride (cell culture tested), Magnesium chloride anhydrous >98%, Ethylenediaminetetraacetic acid disodium salt dehydrate (EDTA), Copper(II) sulfate pentahydrate, cell culture tested >98%, ampicillin sodium salt, ammonium acetate for molecular biology >98%, Amicon Ultra centrifugal filter units (MWCO 10 kDa), sodium chloride for molecular biology >98%, Trizma hydrochloride reagent grade >99% and LB broth powder were purchased from Sigma Aldrich. Apiezon wax sticks were purchased from Edwards. Dpnl and Phusion® High-Fidelity PCR Master Mix (HF Buffer) were purchased from new England Biolabs. QuikChange® Site-Directed Mutagenesis Kit and XL1-Blue Super Competent Cells were purchased from Agilent Technologies. NucleoSpin® Plasmid was purchased from Cultek. Precision Plus Protein™ All Blue Standards was purchased from Bio-rad. Au wire was purchased from Goodfellow. IPTG dioxane-free was purchased from Thermo Scientific. Standard RC Dialysis Tubing (Spectra/Por1, 6-8 kDa) was purchased from Spectrumlabs. D(+)-Sucrosa was purchased from Fluka. HiLoad 26/10 SP Sepharose column was purchased from GE Healthcare Life Sciences. Au(111) single crystals were purchased from Mateck.

2. K41C Azurin mutant

a) Design of the K41C mutant

The plasmid pet3a carrying the gene with the Azurin sequence (Table 1) from *E.Coli* was kindly provided by Dr. Jeff Warren (California Institute of Technology, Pasadena). To synthesize the Azurin mutant K41C, two primers were used in the PCR mutagenesis method. Using the QuikChange® Site-Directed Mutagenesis Kit, both forward and backward primers were designed (Table 2). The mutation of the DNA was conducted following the QuikChange® Kit specifications. The mutated gene was then verified by DNA sequencing (Table 3).

Table 1. Amino acid sequence of the Wt Azurin

Gene	Amino Acid sequence
Wt Azurin	MLRKLAAVSLLSLLSAPLLAAECSVDIQGNDQMVFNTNAITVDKSCQFTVNLSH PGNLPCNVMGHNWVLSTAADMQGVVTDGMASGLDKDYLPDDSRVIAHTKLIG SGEKDSVTFDVSKLKEGEQYMFFCTFPGHSALMKGTLTLK

Table 2. Sequence of the forward and backward primers. The highlighted bases correspond to the ones designed to exchange the K residue by the C residue.

Primer	Amino Acid sequence
K41C_Backward	5'-GTTGTGACCCATAACGTT GCA CGGCAGGTTACCTGGG
K41C_Forward	5'- CCCAGGTAACCTGCCG TGC AACGTTATGGGTCACAAC

Table 3. Sequence of Wt Azurin and K41C mutant. The amino acid 41 is highlighted in both Wt and mutant sequences.

Description	Amino acid sequence
Wt Azurin	AECSVDIQGNDQMVFNTNAITVDKSCQFTVNLSHPGNLP K NVMGHNW VLSTAADMQGVVTDGMASGLDKDYLPDDSRVIAHTKLIGSGEKDSVTFD VSKLKEGEQYMFFCTFPGHSALMKGTLTLK
K41C Azurin	AECSVDIQGNDQMVFNTNAITVDKSCQFTVNLSHPGNLP C NVMGHNWVL STAADMQGVVTDGMASGLDKDYLPDDSRVIAHTKLIGSGEKDSVTFDVSKL KEGEQYMFFCTFPGHSALMKGTLTLK

b) Expression and purification of the K41C mutant

The pet3a vector, including the mutated gene, was used to transform *E.Coli* (BL_21). The plasmid has ampicillin resistance, so all the culture media were prepared with ampicillin to prevent other growing bacteria without our plasmid. One colony was picked and used to inoculate 6 ml of LB (lysogeny broth) medium as starter culture. It was allowed to grow at 37°C until being slightly translucent (4-5 hours). The cultures were span to remove β -lactamase and re-suspended in a fresh 6 ml LB aliquot. It was overexpressed at 32°C overnight (O/N) with vigorous shaking. Then the 6 ml were inoculated to a 500 ml medium and grown at 37°C until the optical density equals 0.6. IPTG (Isopropyl β -D-1-thiogalactopyranoside) is used for the induction of the protein expression and was added to a final concentration of 1 mM. After 5h of induction the cells were harvested by centrifugation and frozen at -20°C O/N. After defrosting, the cells were cracked and the solution has a viscous consistency due to the released DNA. Sonication was used to break genomic DNA and restore a thin consistency. At this point the mutant K41C (a periplasmic protein) remains at the supernatant after centrifugation. The majority of the proteins were precipitated with an acidic solution of 500 mM ammonium acetate (pH 4.5), while our protein is still in solution. The ionic strength was adjusted by dialysis to 25 mM ammonium acetate (pH 4.5). The resultant solution was purified on a HiLoad 26/10 SP Sepharose column (ionic exchange) through a gradient of pH 4.5 - 9 in 25 mM ammonium acetate buffer. At this point, the K41C mutant is completely pure (Figure S1). The metal ions coordinated to the protein were removed by dialysis into a solution containing potassium cyanide, and then the K41C was titrated with a 10 mM $\text{Cu}^+/\text{Cu}^{2+}$ solution. SDS-Polyacrylamide gel electrophoresis (PAGE) was used to follow the protein track and analyse the presence of other proteins (Fig. S1).

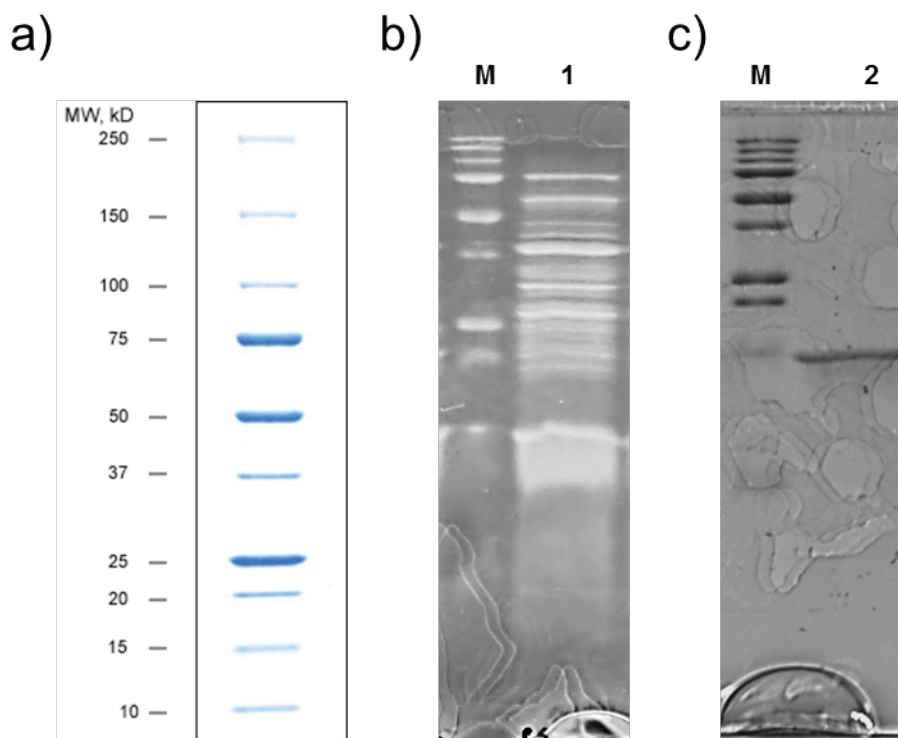


Figure S1 | SDS-PAGE. **a)** Molecular mass standard employed in Lanes M in both **b)** and **c)**. **b)** Lane 1 corresponds to the solution before purification through a HiLoad 26/10 SP Sepharose column. A large fan of proteins are present in the solution. **c)** Lane 2 corresponds to the fraction obtained from the HiLoad 26/10 SP Sepharose column containing the purified K41C. Only a band at 14 KD is seen in that fraction, which corresponds to the K41C protein.

3. Spectroscopic characterization

a) UV-visible spectroscopy

The UV-vis absorption was obtained at room temperature using an Infinite M200 PRO Multimode Microplate Reader from Tecan (Figure S2). Protein samples were solutions of approximately 7 μM in 50 mM ammonium acetate pH 4.5 buffer.

It is known that the Azurin thermal denaturation is irreversible over 84.4°C^1 . Both Wt and K41C variant were heated up to 90°C during 20 minutes to break both tertiary and secondary conformations. UV-vis characterization was then performed to check the disappearance of the Cu^{2+} absorption peak due to the protein unfolding after denaturation (Figure S2a). The structural stability of the protein after mutation is expected to worsen. For this reason, the same test is

performed to elucidate the stability temperature range for the K41C variant (Figure S2b). The folding structure for the K41C variant is stable at temperatures below 70°C.

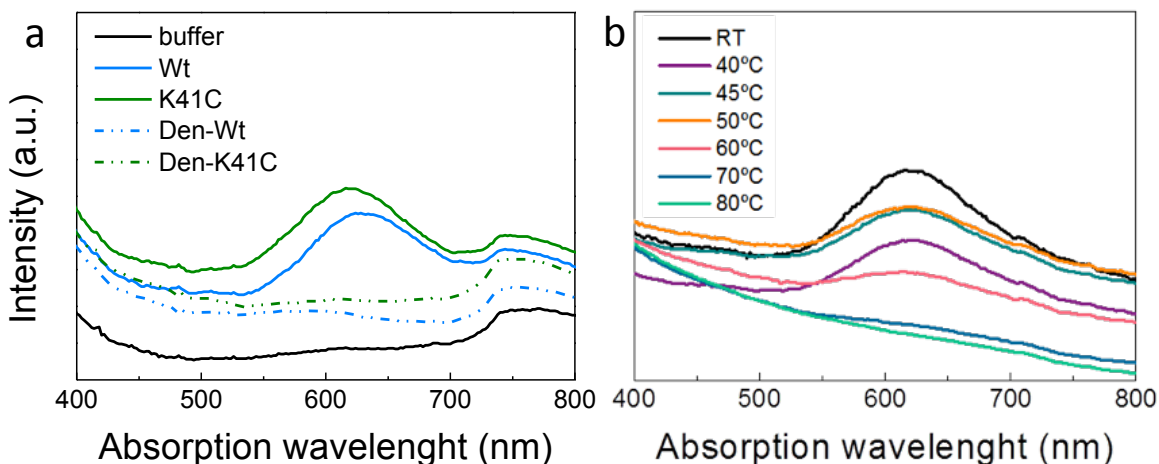


Figure S2 | **a**, Absorption spectra of Wt Azurin (blue line), K41C (green line), denatured-Wt (blue dotted line) and denatured-K41C (green dotted line). Maximum peak absorptions appear at 634 nm and 615 nm for Wt and K41C, respectively. **b**, Absorption spectra of K41C mutant after heating the sample for 10 minutes at increasing temperatures from RT to 80 °C (see legend).

b) Fluorescence spectroscopy

Fluorescence spectra were recorded using a Horiba spectrofluorometer. The fluorescence band of the inner *Trp48* residue was monitored after exciting at 290 nm. The fluorescence peak for the Wt Azurin is centred at 308 nm. This band is characteristic for a completely buried *Trp48* in the protein backbone when the protein folding structure is preserved, and the *Trp48* fluorescence is not quenched by the outer solvent².

Both Wt and K41C variants were measured as well as their denatured counterparts (Figure S3). Both proteins present fluorescent maxima centred around 315 nm before denaturation, which indicates that both proteins preserve the 3D folding structure. After denaturation, the fluorescent peak shifts to ~360 nm, which indicates that the *Trp48* has been exposed to the solvent, evidencing the open structure of the protein. The exact peak values are listed in Table 4.

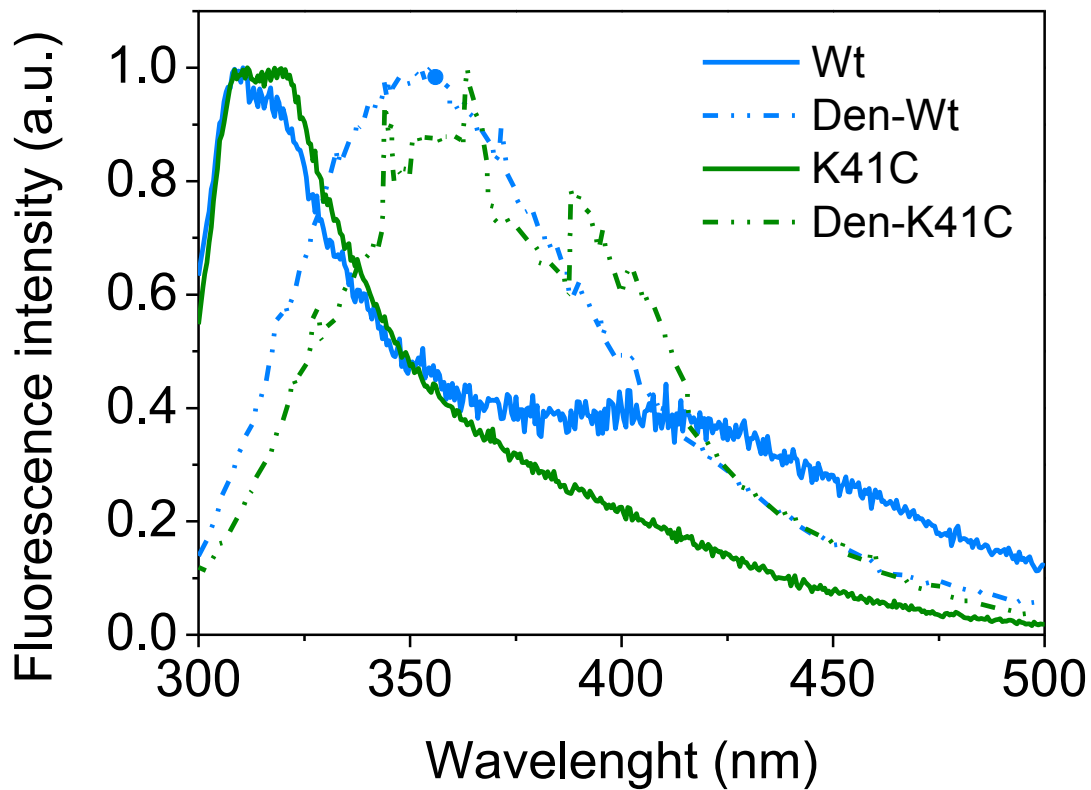


Figure S3 | Fluorescence spectra of Wt Azurin and K41C mutant with the respectively denatured homologous (Den-Wt and Den-K41C). Samples were selectively excited at 290nm.

Table 4. Fluorescence maximum values obtained from Figure S3.

Protein	Fluorescence maximum
Wt azurin	314 nm
Den-Wt azurin	353 nm
K41C	316 nm
Den-K41C	363 nm

4. Electrochemical characterization

a) Sample preparation

A Au(111) single crystal was annealed in a hydrogen flame for 5 minutes. The substrate is allowed to cool down under a nitrogen stream. Then, the electropolishing of the gold surface is conducted by applying 10 V against a Pt mesh cathode during 30" in a 0.1 M sulphuric acid solution. The substrate was rinsed with Milliq water. The oxide formed on the Au surface during the electropolishing stage is removed by immersing the Au(111) crystal for 2 minutes in a 1 M HCl solution. After rinsing with abundant milliq water and drying with an Ar stream, the Au(111) crystal is annealed with a hydrogen flame for 5 minutes again. To conduct the cyclic voltammetry of the proteins, the Au(111) crystal is immersed in a 10 mM hexanethiols solution overnight. Then, it is rinsed with abundant ethanol and water several times to remove the non-covalently bound hexanethiols. The functionalized Au is covered with a droplet of 50 mM ammonium acetate pH 4.5 buffer containing Wt, K41C, den-Wt or den-K41C proteins (denaturation is performed at 90°C), and allow them to adsorb for at least 2 hours. The Wt and K41C proteins attach to the hexanethiols by its hydrophobic patch near the copper ion (Figure S4a)³.

b) Cyclic voltammetry (CV)

Voltammograms were undertaken using an Autolab PGSTAT-12 Galvanostat-Potentiostat. The electrochemical cell is composed by a platinum wire as the counter electrode, a miniaturized ultralow-leakage membrane Ag/AgCl (SSC) as the reference electrode, and the CH₃(CH₂)₅S-Au(111) as the working electrode. All the electrolytes solutions were deoxygenated with purified argon. Cyclic voltammograms were done at a scan rate of 50 mV·s⁻¹. The experiments were performed in 50 mM ammonium acetate buffer pH 4.55.

Fig S4a shows a scheme of the protein adsorbed onto the alkanethiol SAM that was used to record the CVs. As previously reported³, Azurin has a hydrophobic patch near the copper centre that allows direct interaction with the methyl end of the alkanethiols, facing the copper centre to the electrode surface. It has been proven that Azurin proteins in this configuration are redox active³. The extracted redox midpoints from the CVs for the Wt and K41C are 120 mV and 172 mV respectively.

CVs of denaturated proteins were also performed to prove that unfolded proteins have no redox activity. Figure S4b-c shows that there is no redox activity for both Wt and K41C denaturated proteins (no peaks were observed in the corresponding CVs).

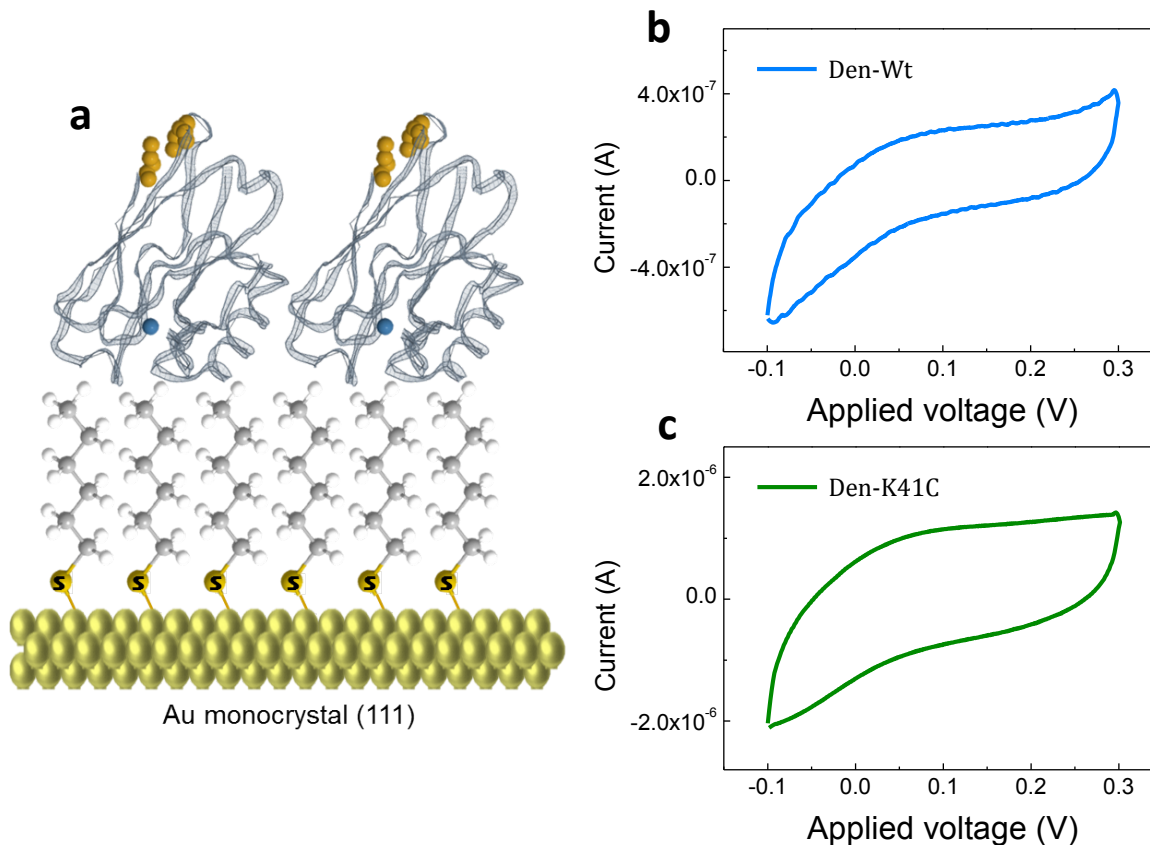


Figure S4 | a, Schematic representation of the protein adsorption on a hexanethiol-functionalized Au(111) electrode. b-c, Cyclic voltammograms of denaturated Wt Azurin (Den-Wt, blue line) and denaturated K41C (Den-K41C, green line) respectively on the hexanethiol-functionalized Au(111) electrode in 50 mM ammonium acetate buffer, pH 4.55. Scan rate $50 \text{ mV} \cdot \text{s}^{-1}$.

5. Electrochemical Scanning Tunnelling Microscopy (ECSTM)

a) Sample preparation

A Au (111) crystal was annealed in a hydrogen flame for 5 minutes. The substrate is allowed to cool down under a nitrogen stream. Then, electropolishing of the gold surface is conducted by applying 10 V against a Pt mesh cathode during 30'' in a 0.1 M sulphuric acid solution. The substrate was rinsed with Milli-Q water. The oxide formed on the Au surface during the

electropolishing stage is removed by immersing the Au(111) crystal for 2 minutes in a 1 M HCl solution. After rinsing with abundant Milli-Q water and drying with an Ar stream, the Au(111) crystal is annealed with a hydrogen flame for 5 minutes again. For the STM measurements the protein solution was directly adsorbed to the freshly prepared Au(111) surface after the last annealing and allowed for a 2h incubation. In this case, the Azurin is covalently bound to the Au surface through the two natural Cysteine residues, Cys3 and 26 (see SI section 7 and manuscript discussion).

b) EC-STM measurements

-Methodology:

All experiments were performed with a PicoSPM microscope head and a PicoStat bipotentiostat (Agilent, USA) controlled by a Dulcinea electronics (Nanotec Electronica, Spain) using the WSxM 4.13 software. Two different cells were required; a liquid cell with standard sample plate for the room temperature measurements and a Peltier (Cold MAC) sample plate for temperature control experiments. A four-electrode cell is required for the bipotentiostatic control: a Pt:Ir (80:20) wire as the counter electrode, a miniaturized ultralow leakage membrane Ag/AgCl (SSC) as the reference electrode, and two working electrodes; the Au(111) substrate and a STM probe, whose potentials U_{sample} and U_{tip} , respectively, are expressed against the same Ag/AgCl reference electrode. All glass and Teflon material required for solutions and sample preparation was cleaned with piranha solution (70:30 H_2SO_4 : H_2O_2 by volume). A 50 mM ammonium acetate pH 4.55 buffer was used for the measurements, previously filtered and deoxygenated with an Ar stream. The EC-STM probes were mechanically cut from a 0.25 mm diameter Au wire (99.99%) and they are made of 1 cm in length, annealed with a butane flame and coated with Apiezon wax to minimize leakage current when immersed in the working aqueous buffer. The leakage current of our tips was typically of <10 pA. A NI-DAQmx and BNC-2110 LabVIEW setup was used for data acquisition, and Origin and LabVIEW software were used for analysis. Two EC-STM methodologies were used to study the conductance of the single-protein junctions: the dynamic STM break-junction method (STM-BJ) and the static “*blinking*” STM method. Both approaches were used to generate 1D conductance histograms whereas the *blinking* approach was used for 2D maps only. Shortly, in STM-BJ – a dynamic mode - the probe is approach to a tunnel distance from the sample and the feedback loop is turned off. Through a LabVIEW routine, a voltage is applied to the piezo so the STM tip is withdrawn and approached to the

sample in order to form and break the contact between the STM tip and the Au substrate (Fig. S5). Current distance curves were recorded during the withdrawing stage, with only ~20% of them bearing steps or plateaus corresponding to the formation of a single-protein junction. The conductance value of the single-protein junction is calculated through the expression $G=I_{\text{step}}/U_{\text{bias}}$. The ramps containing steps are used to construct the 1D histogram where a peak will represent the most probable single-protein conductance value. In contrast, in the “blinking” method – a static mode – the probe is set at tunnel distance from the sample and the feedback is turned off after a period of mechanical stabilization. Current versus time traces are then recorded in packets of few seconds during a total time of several hours. When a protein spans the STM tip-substrate gap, a “jump” or “blink” is observed in the current transient in the form of telegraphic noise (Fig. S6). Likewise, the current is transformed in conductance value of the single-protein junction using $G=I_{\text{blink}}/U_{\text{bias}}$. Up to a hundred of such *blinks* are used to build 2D *blinking* maps and its corresponding 1D conductance histogram without any data selection.

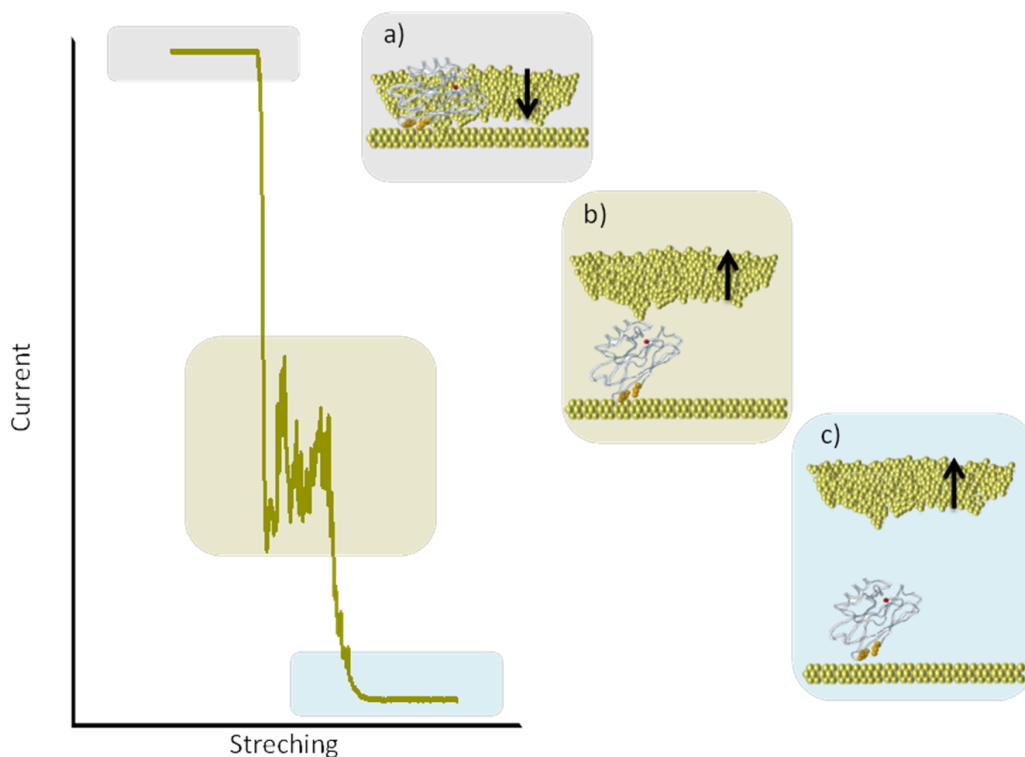


Figure S5 | Scheme of a dynamic break junction (STM-BJ) experiment: a) tip approaching to the surface until a maximum feedback current is reached that sets the minimum STM tip-Au substrate separation; b) single molecule junction between tip and substrate. As the STM probe withdraws from the

sample, chances are that a protein bridges and a plateau in the current shows up; **c)** the single-protein junction is broken and the current decays exponentially till zero as the tip goes out of the tunnelling range.

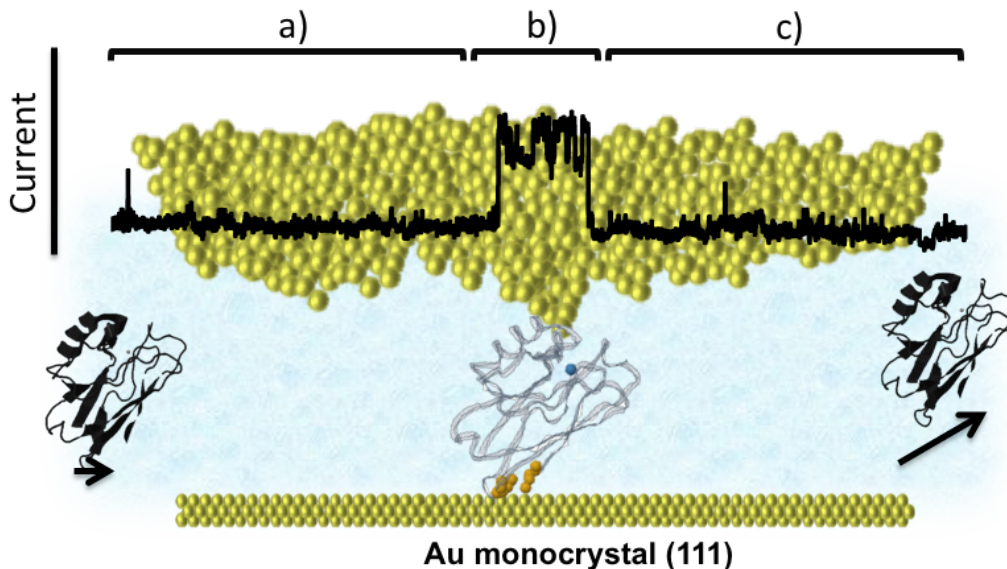


Figure S6 | Scheme of a *blinking* experiment: **a)** the STM tip is set at a tunnelling distance from the Au substrate (initial setpoint tunnelling current) and the current feedback control is switched off; **b)** a protein bridge is established between the STM tip and the substrate with the corresponding change in the current ("*blink*"); **c)** the protein bridge eventually breaks and the current goes back to the initial tunnelling setpoint value.

-Single Protein imaging:

To avoid interferences from protein-protein interactions, we have used low protein coverage of the Au(111) substrate in the single-protein junction experiments. To test the protein surface coverage, EC-STM imaging is performed prior to each single-protein junction experiment to control the amount of proteins on the Au(111) electrode surface (see Figure S7).

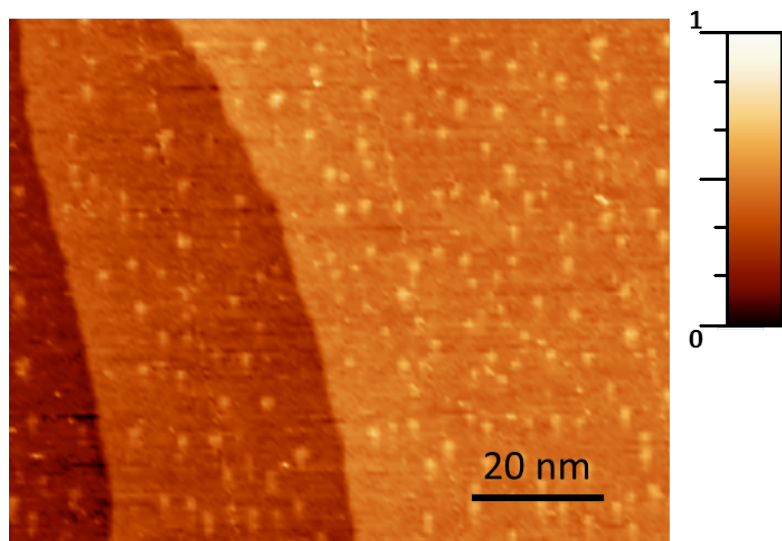


Figure S7 | EC-STM image of a Wt Azurin-functionalized Au(111) surface in 50 mM ammonium acetate pH 4.5. The image was recorded at $U_{\text{sample}} = 0.2$ V and constant V_{bias} of 0.3 V. The Z scale is 1 nm.

-1D histograms from 2D *blinking* maps:

Figures S8 and S9 are Fig. 3b and 4 from the manuscript accompanied with the corresponding 1D histograms from each 2D *blinking* map. The G values represented in the far left graphs were obtained from Gaussian fits of the 1D histogram peaks and the error bar correspond to the FWHM of the same fits.

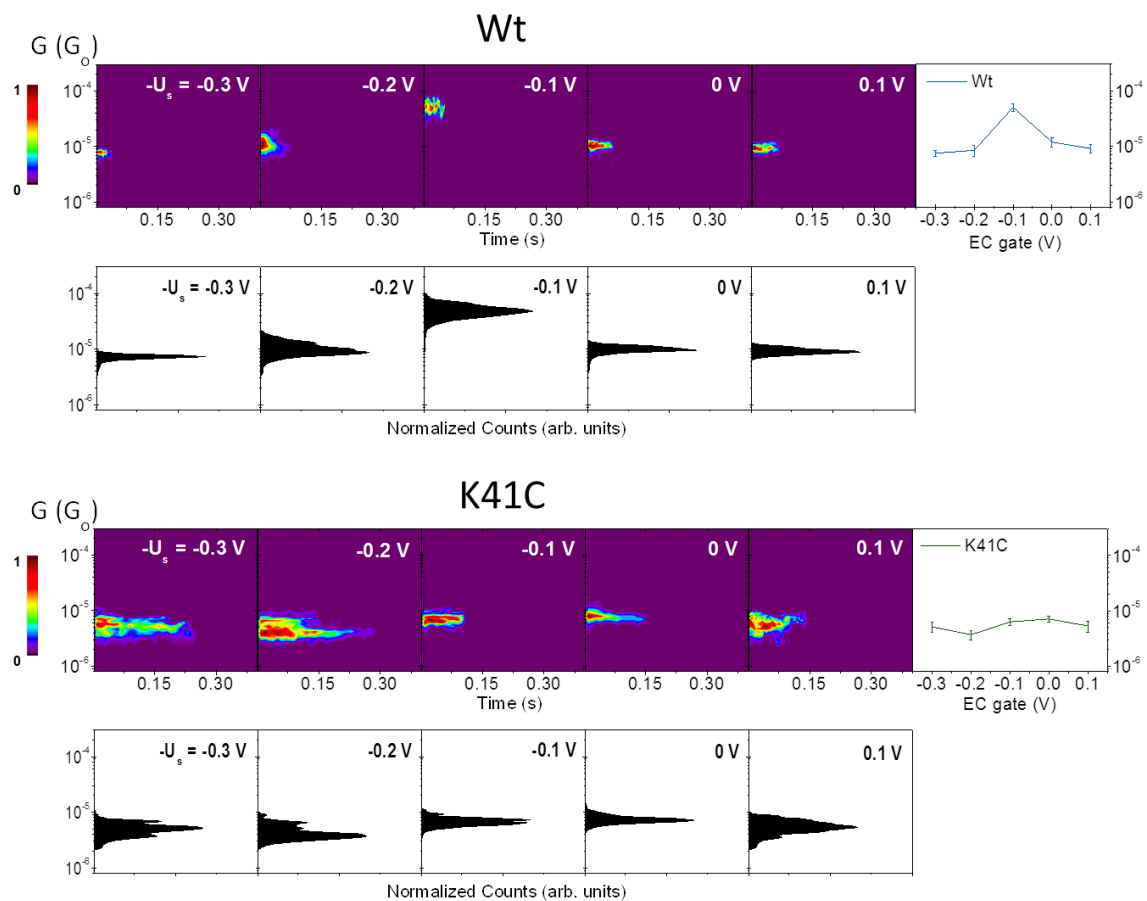


Figure S8 | 1D histograms for each corresponding 2D *blinking* map is added to the same Figure 3b in the manuscript.

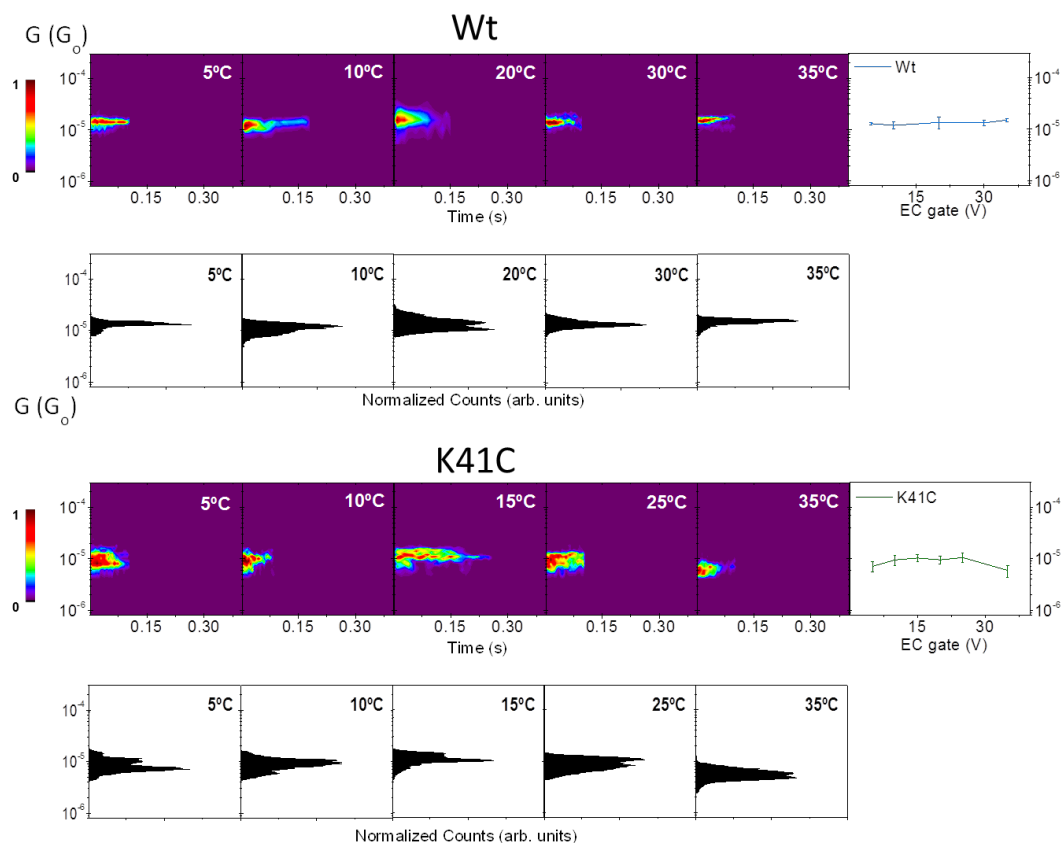


Figure S9 | 1D histograms for each corresponding 2D *blinking* map are added to the same Figure 4 in the manuscript.

-Blinking at large electrode-electrode gap separations:

In order to corroborate that the observed *blinks* correspond to individual protein trapping events, larger electrode-electrode separations were imposed by retracting the STM tip electrode 2 nm further away from the distance set by the initial tunnelling current setpoint (~ 1.5 nm). We observe that the large protein backbone is still capable of closing the larger electrode-electrode gap separation (~ 3.5 nm) resulting in a similar telegraphic signal in the *blinking* experiment (Figure S10).

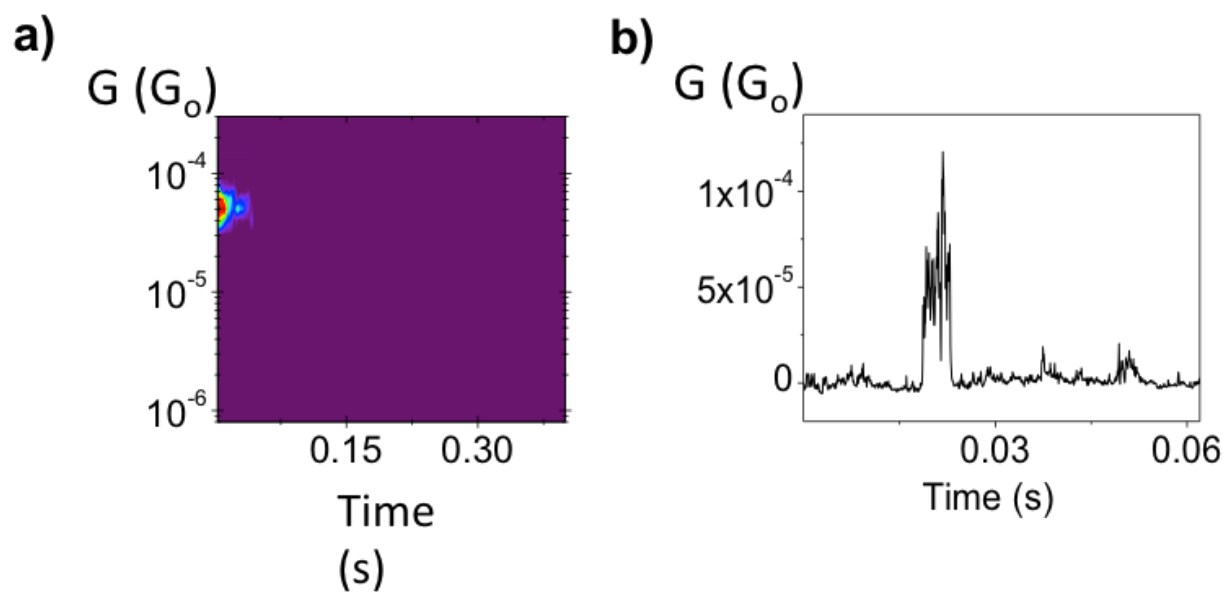


Figure S10 | **a**, 2D-blinking map obtained for the single-protein Wt junction at an EC gate of -0.1 V (constant V_{bias} of 0.3 V). The tip was retracted 2 nm from the surface from the initial setpoint tunnelling distance (~ 1.5 nm). **b**, A representative *blink* obtained after retracting the STM tip electrode.

-Blinking control experiments:

Additional control *blinking* experiments were conducted to ensure that no conductance *blink* is obtained apart from those coming from folded proteins spanning the STM gap. *Blinking* current traces were recorded for three control samples: 50 mM ammonium acetate buffer pH 4.55 without any protein, denatured-Wt (Den-Wt) and denatured-K41C mutant (Den-K41C) both in the same buffer. Up to a hundred traces extending in an equivalent time period like those recorded in Figure 3b and 4 were recorded. In the three cases, no apparent “*blinks*” were observed (Figure S11).

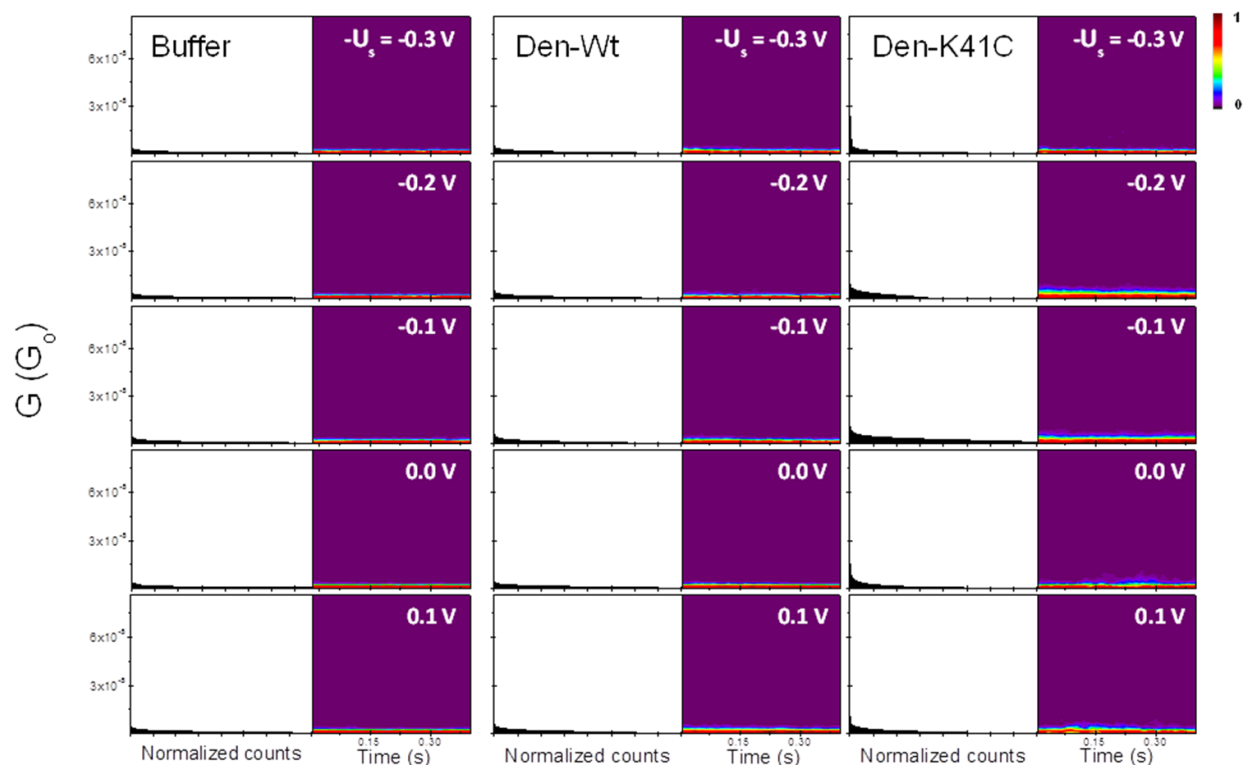


Figure S11 | Control *blinking* measurements. Two different histograms are shown for each of the three measured samples: 1D conductance histograms (left panel) and the corresponding 2D *blinking* map (right panel). Buffer (left), Den-Wt (centre) and Den-K41C (right) correspond to protein-free 50 mM ammonium acetate buffer pH 4.55, denaturated-Wt and denaturated-K41C (both in the same buffer) respectively. The histograms were recorded at different EC gate, constant V_{bias} of 0.3 V and a tunnelling distance of ~ 1.5 nm. Both 1D and 2D graphs have normalized counts being the maximum count level set to 1.

-Blinking of Apo-proteins:

In order to evidence the role of the Cu centre in the charge transport through the single-protein junction, we have recorded blinking traces as a function of the EC gate for the apo-Wt and apo-K41C mutant, both lacking the Cu centre in their structure (see Fig. S12). The conductance invariance against the EC gate in both cases evidences the direct involvement of the Cu centre in the two-step sequential tunnelling in the former case, as well as the poor participation of the Cu centre in the mutated protein case.

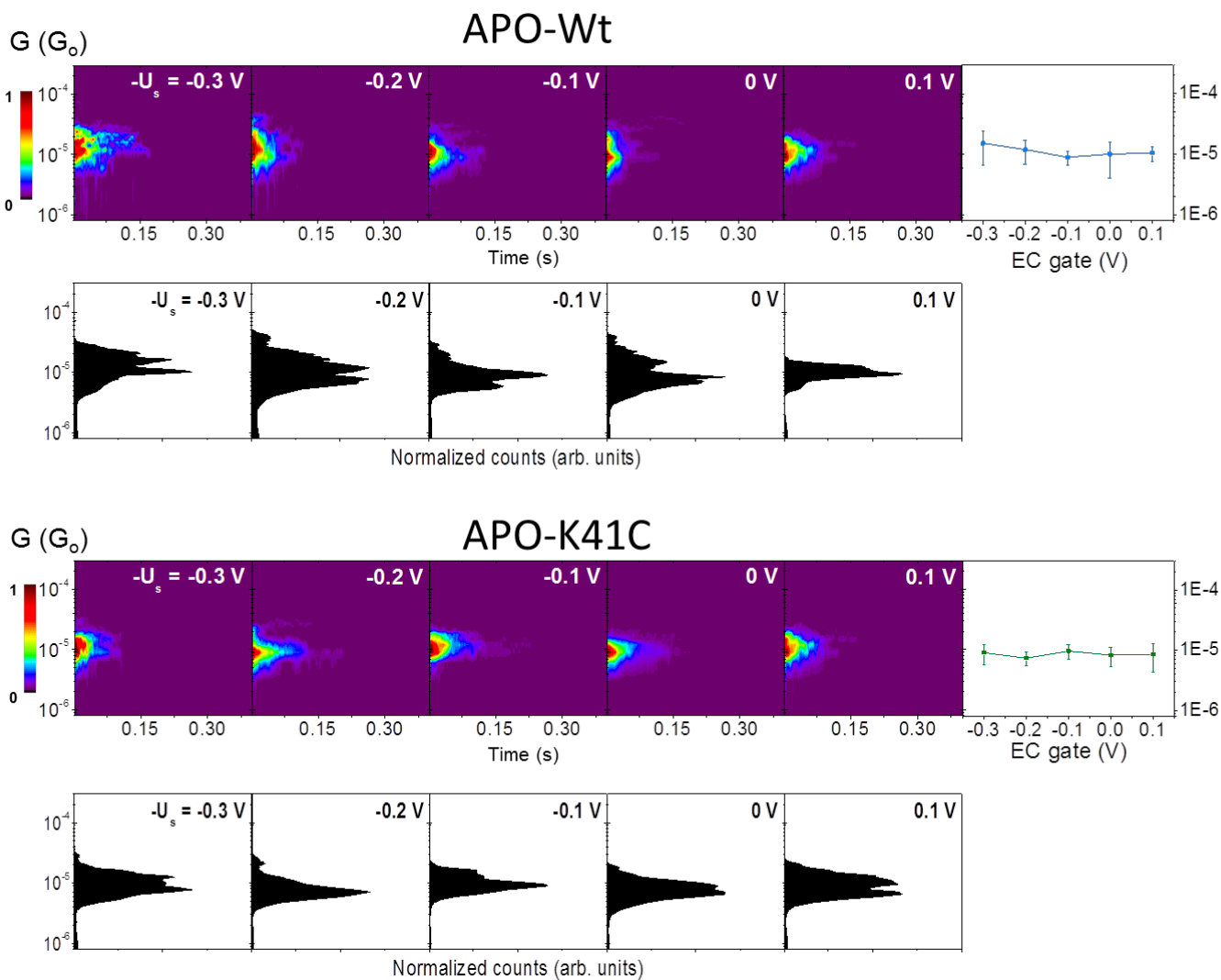


Figure S12 | Gate-dependent single-APO-proteins junction transport. Conductance behaviour versus EC gate ($-U_{\text{sample}}$ in our EC-STM configuration) at constant V_{bias} of 300 mV and tunnelling distance of ~ 1.5 nm for the APO-Wt and APO-K41C. 2D *blinking* maps (top) and 1D histograms (bottom) are shown for each of the two proteins. The counts have been normalized for each map versus the maximum value so each 2D map has its maximum count set to 1. The far right graph summarizes the single-protein conductance (G) vs. the EC gate for both studied proteins. The conductance values were obtained from the Gaussian fit maxima of the 1D histogram. The error bars in these plots are extracted from the full width half-maximum (FWHM) of the Gaussian fits.

-Analysis of the Single-protein junction lifetimes:

The *blinking* experiments allow analysis of the mechanical stability for all the studied single-protein junctions. Figures S13 and S14 show histograms of the extracted lifetime from each 2D *blinking* map (X-axis) recorded for the Wt and K41C variant (Fig. S13) and both corresponding apo (no Cu) proteins (Fig. S14). The lowest scored values correspond to the apo-proteins, which points toward a mechanical stabilization role of the Cu centre as previously reported⁴. Likewise, the single-protein junction built with the holo proteins (with Cu centre) scores larger lifetimes. Interestingly, the mutation introduced at the second coordination sphere of the Cu centre in the K41C mutant brings enhanced mechanical stability of the single-protein junctions (significantly larger lifetimes) thanks to the additional thiol anchoring group introduced at the bioengineered Cys residue at position 41. The larger bridging capabilities of the K41C mutant are also evidenced in the TEM experiments presented in the next section 6.

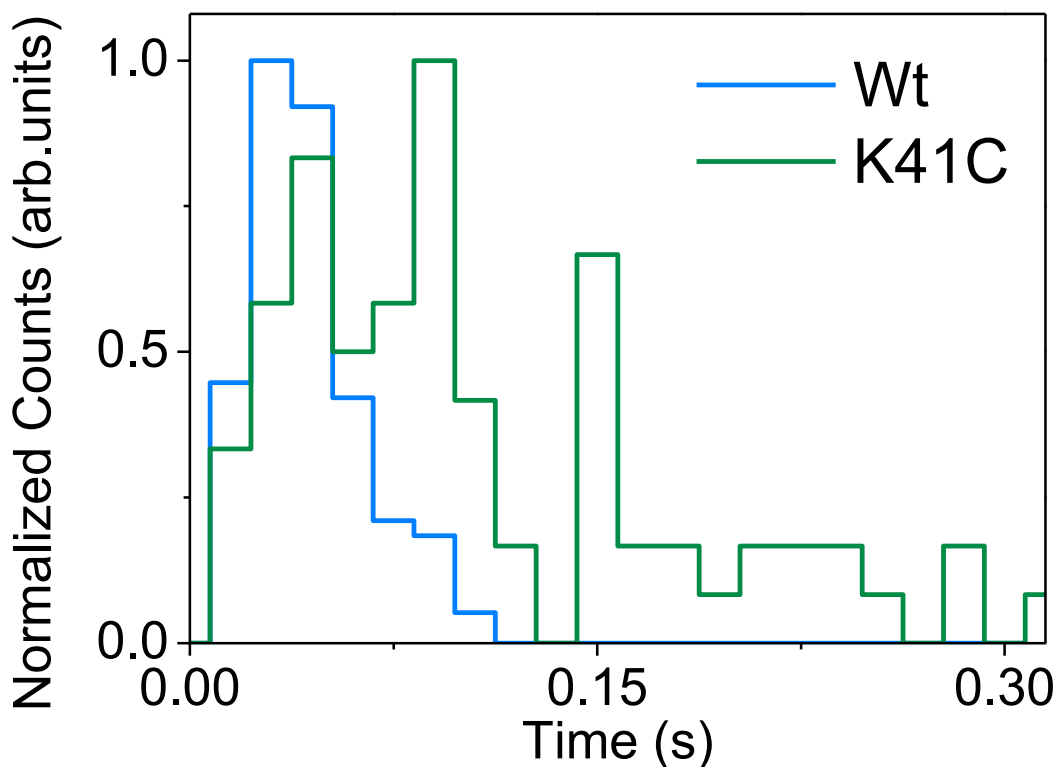


Figure S13 | The lifetimes of the observed *blinks* for Wt (blue line) and K41C (green line) are represented. All the *blinking* traces from the gate dependent single-protein transport were included in the calculation. The counts of both Wt and K41C were normalized.

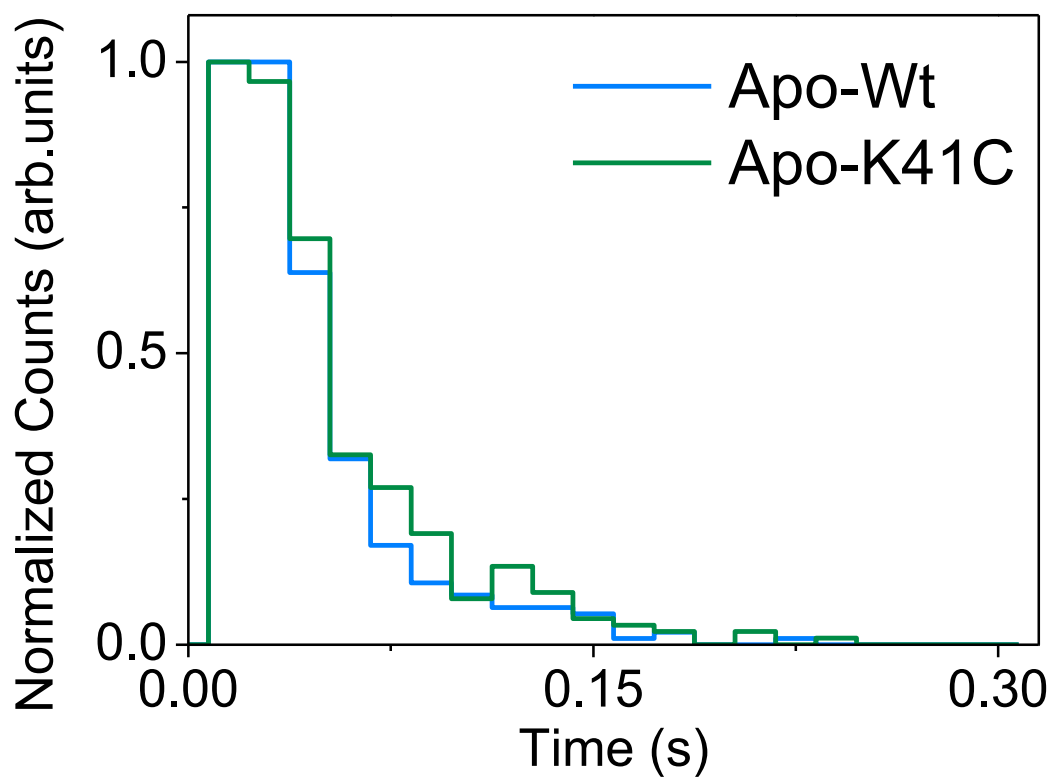


Figure S14 | The lifetime of the observed *blinks* for Apo-Wt (blue line) and Apo-K41C (green line) are represented. All the *blinking* traces from the gate dependent single-protein transport were included in the calculation. The counts of both Apo-Wt and Apo-K41C were normalized.

6. Transmission electron microscopy (TEM)

In order to confirm the bridging efficiency of the extra thiol anchoring point in the K41C variant versus the Wt, three different systems were studied by TEM: i) free-protein Au Nanoparticles (NP); ii) Au NP-Wt (10:1 molar); iii) Au NP-K41C (10:1 molar). The solutions were prepared by having a low NP concentration of $2.8 \cdot 10^{+13}$ NP/ml suspended in the working buffer with and without the proteins for a period of 2 hours (we use the same incubation time as for the STM samples). 3 μ l of solution was then deposited over a TEM gold grid till it completely dries, after what, the surface was washed several times with additional freshly prepared free-protein buffer. Both proteins covalently binds to Au NP through the two natural Cysteine residues (Cys3 and Cys26)⁵. Large numbers of TEM images (N~10) were taken for each system and the percentage of Au NPs dispersion/aggregates was calculated through imaging analysis software. As shown in Figure S15a and Table 5, the percentage of NP dimers formation is significantly larger in the case of the K41C, ~20%, than in the Wt case, ~13%, and the presence of both proteins favour in general the NP interconnection. The K41C is the only one capable of forming large NP networks (number of NP>5) at the very low employed concentrations (see far left panel in Fig. S15). These observations support the fact that the K41C variant presents enhanced capability to bridge two NP through their two axial thiol (-SH) groups, namely, the two natural Cys3 and 26 and the bioengineered Cys41. These results also support the measured enhanced lifetime of the single-protein junction for the K41C (Fig. S13).

Figure S15b and c show both EDS spectrums of NP-Wt and NP-K41C samples. They were taken on a small region covering few NPs. It is clearly seen that a peak for Cu appears, which indicates the presence of protein (the only source of Cu). The gold peak corresponds to the NPs as well as the TEM grid.

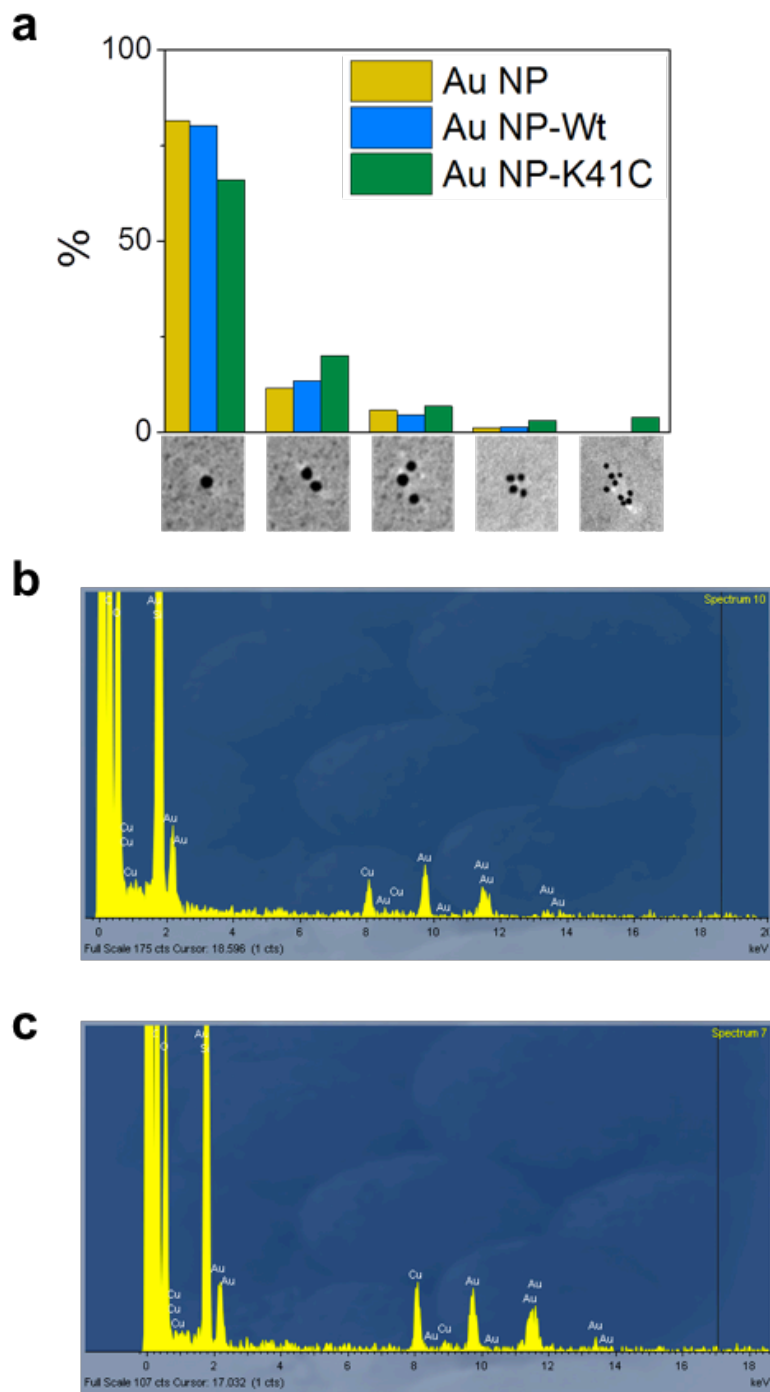


Figure S15 | Transmission electron microscopy (TEM). The percentages (%) of Au NPs dispersion/aggregates (single NP, two NP, three NP, four NP, >five NP) were calculated for the three studied samples: free-protein Au NP (yellow), Au NP incubated with Wt protein (blue) and Au NP incubated with K41C variant (green). **b**, EDS spectrum of Au NP-Wt (10:1) and **c**, EDS spectrum of Au NP-K41C (10:1), both performed on a gold grid.

Table 5. Percentages (%) of Au NPs aggregates (single NP, two NP, three NP, four NP, >five NP network).

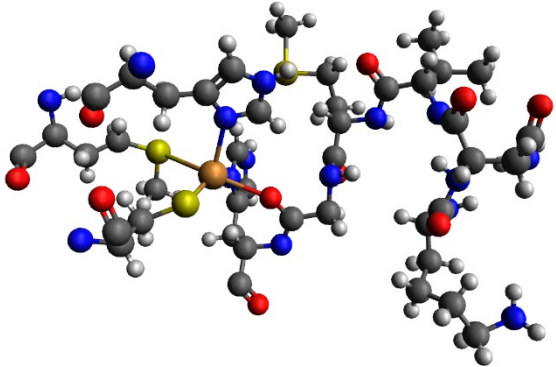
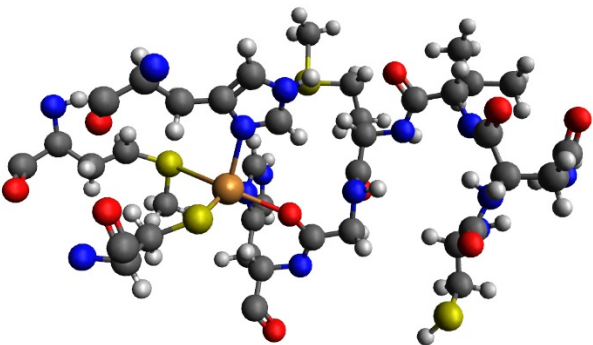
	1 NP	2 NP	3 NP	4 NP	≥5 NP
Au NP	81.5 %	11.6 %	5.8 %	1.1 %	0 %
Au NP-Wt	80.3 %	13.5 %	4.5 %	1.5 %	0.2 %
Au NP-K41C	66 %	20.1 %	6.8 %	3.2 %	3.9 %

7. Computational methods

a) Visualization of the frontier orbitals and calculation of their energies for the studied protein fragment.

The geometry of for studied Wt Azurin was obtained from the PDB (<http://www.rcsb.org/pdb/explore/explore.do?structureId=1AZU>). In view of our spectroscopic results and molecular dynamics simulations (see manuscript), the K41C fragment structure was assumed to be the same as the 1AZU by replacing the *Lys41* for a *Cys41*. The calculated frontier orbitals for both molecules were obtained using *Density Functional* methods (DFT) using the software package *Gaussian 09*⁶. To predict correctly^{7,8} the electron-transport pathways,⁹⁻¹¹ a long-range-corrected variant *CAM-B3LYP* method was applied¹²⁻¹⁶ using *6-311G+(d)* as basis set. All isosurface plots were obtained using *Avogadro* visualizing software¹⁷.

Similar to QM/MM treatments, the *ab initio* calculations were conducted in the relevant fragment of the protein for the electron transport: 41-45, 46, 112, 117, 121 and 129.

(a) Protein fragment	HOMO	LUMO
Wt Azurin 	-7.26 eV	-6.64 eV
K41C mutant 	-7.46 eV	-6.01 eV

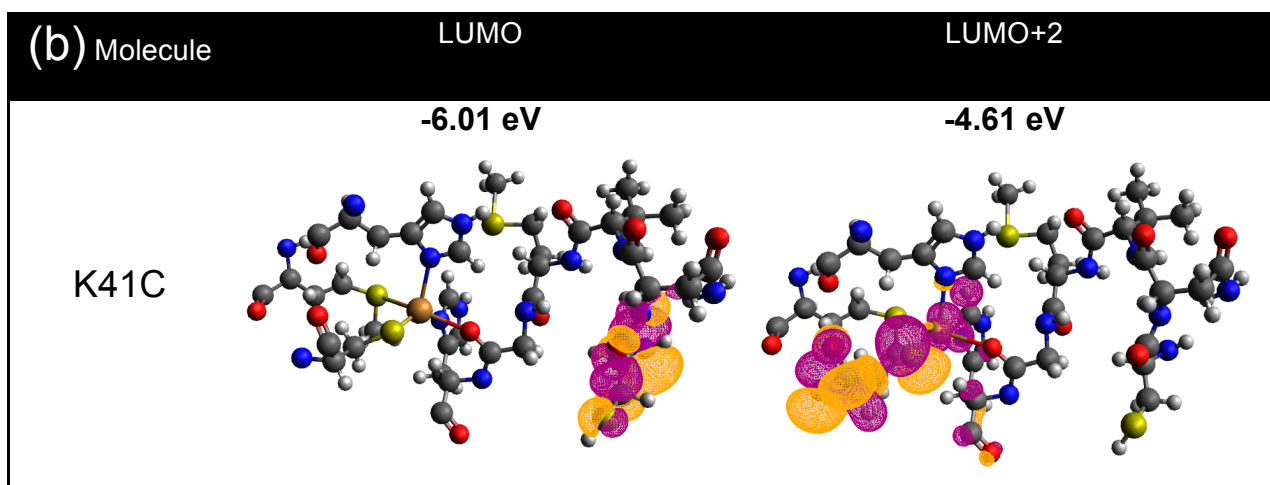


Figure S16 | **a**, Molecular representations of the Wt and K41C and their calculated frontier orbitals energy. **b**, LUMO and LUMO+2 visualization and energies of the K41C. All calculations were done at the CAM-B3LYP/6311G+(d) level of DFT.

b) Molecular Dynamics Simulations

-Simulation details:

Here we report the supporting Molecular Dynamics (MD) simulations results which allow us to: 1) quantitatively describe the structural changes on the WT-Azurin introduced by the K41C mutation; 2) identify the possible adsorption conformations of the WT-Azurin over the Au(111) surface, and subsequently quantify the structural changes induced by such process; 3) understand the influence of a gold STM tip on the structural stability of the Wt-Azurin as a function of the tip indentation height. In what follows, we provide the technical details associated with the MD simulations, which are common to all these sub-sections.

All the simulations were performed using the AMBER14 software suite¹⁸ with NVIDIA GPU acceleration¹⁹⁻²¹. The parmbsc0 modification²² of the Cornell ff99 force field²³ was used to describe all standard amino acids present in the Azurin. The inter-atomic potentials of the copper atom and its corresponding 5 ligands were described using a force field derived from quantum mechanical simulations²⁴. This force-field, has been widely used to model the blue-copper Azurin protein²⁵⁻²⁸. In particular, recent experiments²⁶ have shown how early stages of mechanical unfolding of this protein are well described by this force-field. In all our simulations, the system is fully embedded in a water medium. The water is described using explicit TIP3P model²⁹, while Joung/Cheatham parameters were used to describe the sodium counter-ions^{30,31}. For the gold atoms we have resorted to CHARMM-METAL force-field^{32,33}, since it is thermodynamically consistent with the AMBERFF used to describe the protein and it has been successfully employed to study inorganic-bioorganic interfaces³³. We have used periodic boundary conditions and Particle Mesh Ewald (with standard defaults and a real-space cutoff of 10 Å) were used to account for long-range electrostatic interactions. Van der Waals contacts were truncated at the real space cutoff of 10 Å for all the simulations also. SHAKE algorithm was used to constrain bonds containing hydrogen, thus allowing us to use an integration step of 2 fs. Coordinates were saved every 1000 steps.

The X-ray crystallographic structure of Azurin was obtained from the protein data bank (PDB)³⁴ with the PDB code 4AZU³⁵. Protons were added to the protein structure according to the calculated ionization states³⁶ of its titratable groups, at a pH of 4.5, which corresponds to the one used in the experiments. The resulting structure net charge was zero for Wt-Azurin (with and without the copper atom) and -1 for the mutant K41C. The gold surface used to study the protein adsorption is a (111) surface (along z direction, *i.e.* the direction perpendicular to the surface) with dimensions of 8x8 nm² (see Fig S17e) along the xy plane and a thickness along the z

direction of three atomic layers. In all simulations the gold atomic positions are weakly restrained (with a positional elastic constant of 5Kcal/mol). Note that we have performed one simulation where the gold atoms are unrestrained and we found no difference on the adsorption with respect to the restrained case. At last, the gold tip used to perform the indentation has a radius of 2 nm and the (111) planes are perpendicular to the indentation direction.

For all the simulations here shown the protocol essentially consists of three stages: 1) structures were energy minimized to avoid steric clashes using a combination of steepest descent and conjugate gradient methods; 2) then, given that all the simulations are performed in a liquid medium, we perform a 2 ns simulation in the NPT ensemble, *i.e.* keeping the pressure constant at 1 atm and the temperature constant at 300K; 3) at last, given the stabilization of the pressure to 1 atm in the simulation box, and the higher computational cost associated to the NPT simulations with respect to the NVT simulations (Number of atoms, Volume and temperature are fixed), the production MD runs were performed in the NVT ensemble.

-MD simulations of Azurin in water: structural differences/similarities between Cu-Azurin, Wt and K41C mutant:

In this section we access the structure stability of three different Azurin structures: Wt, K41C mutant and Apo (without the copper), which are freely floating in a water solution at a pH of 4.5. In Fig S17, we show the initial configurations of the Wt (Fig 17a), K41C (Fig 17b) and Apo (Fig 17c). In Fig 17d, the Cu-Azurin is represented with a Connolly surface where the residues are colored in agreement with their hydrophobicity index. In this figure, one can clearly observe the protein hydrophobic patch (in dark blue), which is located near the copper atom.

We have analysed the dynamics of the Wt and the K41C structures during 500 ns of NVT simulations, and the dynamics of the Apo structure during 300 ns. Looking at the time evolution of the total energy for the three Azurin structures in Fig S18a), one realizes that in all cases a thermal equilibrium is reached before the 200ns of MD simulation. In Fig S19 we represent the final configurations of the three structures obtained at the end of the dynamics. From this figure, we realize that all molecules seem to preserve its initial structure, in particular the mutation seems to have no effect on the overall structure of the protein. This can be quantified by looking at the evolution of the radius of gyration and the root-mean-square deviation (R_g and RMSD respectively, see Fig S18) that are practically identical for the Wt and for the K41C. The

same happens to the secondary structure, whose time evolution is shown in Fig S20, *i.e.* for both molecules we observe an identical content of alpha-helices and beta-sheets as well as their changes induced by the thermal fluctuations occurring during the dynamics.

Concerning the Apo structure, the same arguments exposed before for the mutant K41C apply, *i.e.* one barely notices any structural change with respect to the Wt.

In summary, our molecular dynamics simulations for the free molecules indicate that both the structure and the dynamics of these three molecules are very similar. This conclusion is better seen in Fig S21, where the aligned final configuration of the Wt and K41C structures (a) as well as the Wt and Apo structures (b) clearly show that structurally all these molecules are very similar.

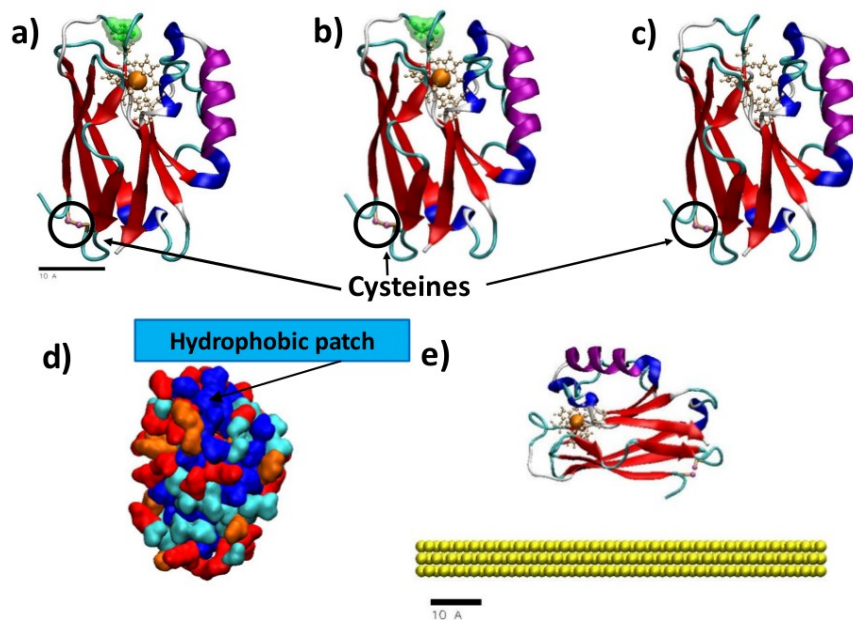


Figure S17 | Initial configurations of the (a) Wt, (b) K41C and (c) Apo structures. The Azurin is represented with its secondary structure: betasheets (red), alpha-helix (purple), 310- helix (dark-blue), turns (cyan), and random-coils (white). The copper atom is shown using its Van- der-Waals representation in an opaque orange color, and its coordination residues are represented with ball-stick model in a metallic-pastel orange color. The disulfide bridge is shown in a bond representation colored in light orange, and the main chain of two cysteines, which formed it are colored in pink. Moreover, the position of the residue in which the mutation has been performed (Lysine replaced by a Cysteine) has been marked with a green Connolly surface³⁷. (d) Residue distribution for all the Azurin structures colored

in accordance with their hydrophobicity index: very hydrophobic (blue), hydrophobic (cyan), neutral (orange), and hydrophilic (red) residues. The orientation of the protein is the same as in a)-c). The Hydrophobic patch (near de cooper atom) of the protein is marked with a blue rectangle. **(e)** Representation of the configuration of the Cu-Azurin over the whole gold surface for one of the orientation studied (O1).

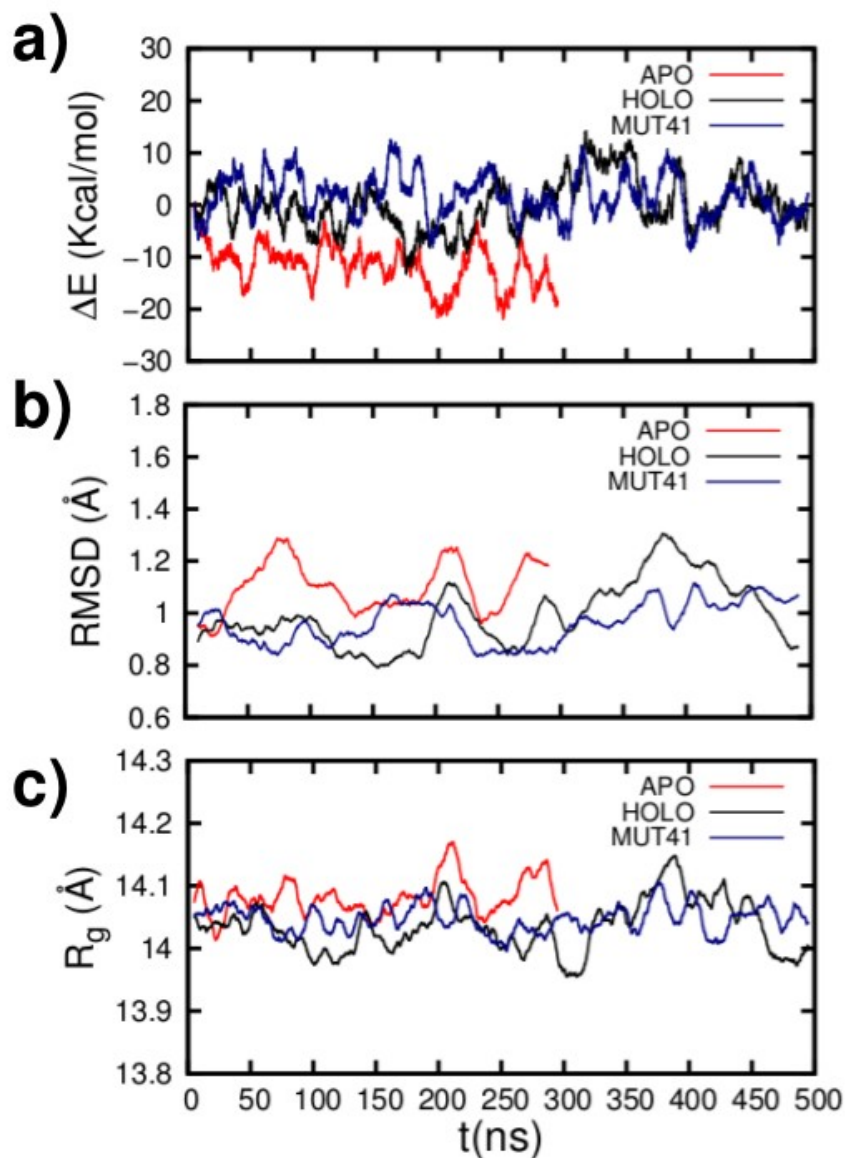


Figure S18 | Evolution of the total energy change (top), the root-mean-square deviation, RMSD, (middle) and the radius of gyration, R_g , (bottom) for the Apo (red), Wt (black) and K41C (blue) structures during the simulation of its free dynamic in solution. The average of the total energy in the first

10 ns has been taken as our energy reference. RMSD has been calculated for all the backbone atoms of the protein. The Apo results go only until 300 ns as this simulation is shorter than the other two.

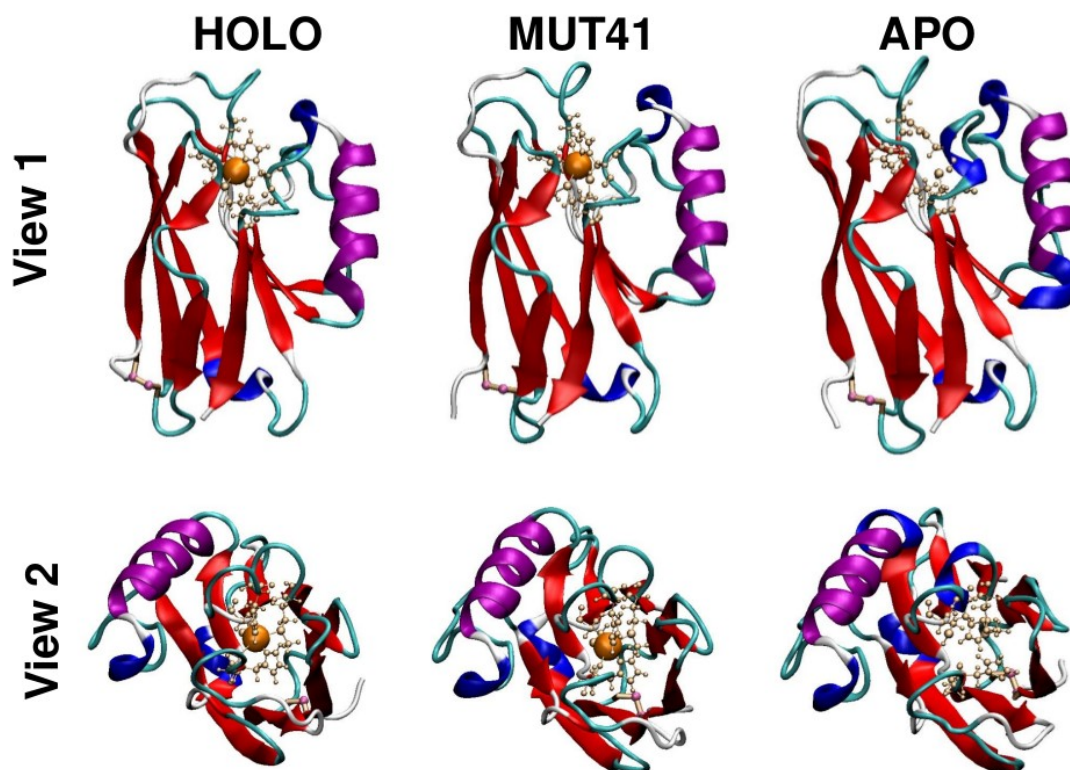


Figure S19 | Final configurations obtained at the end of the simulation for the Apo (300 ns), Wt (500 ns) and K41C (500 ns) structures. Two different views of the protein are shown for each structure. The color representation used for the protein is the same as in Fig S17

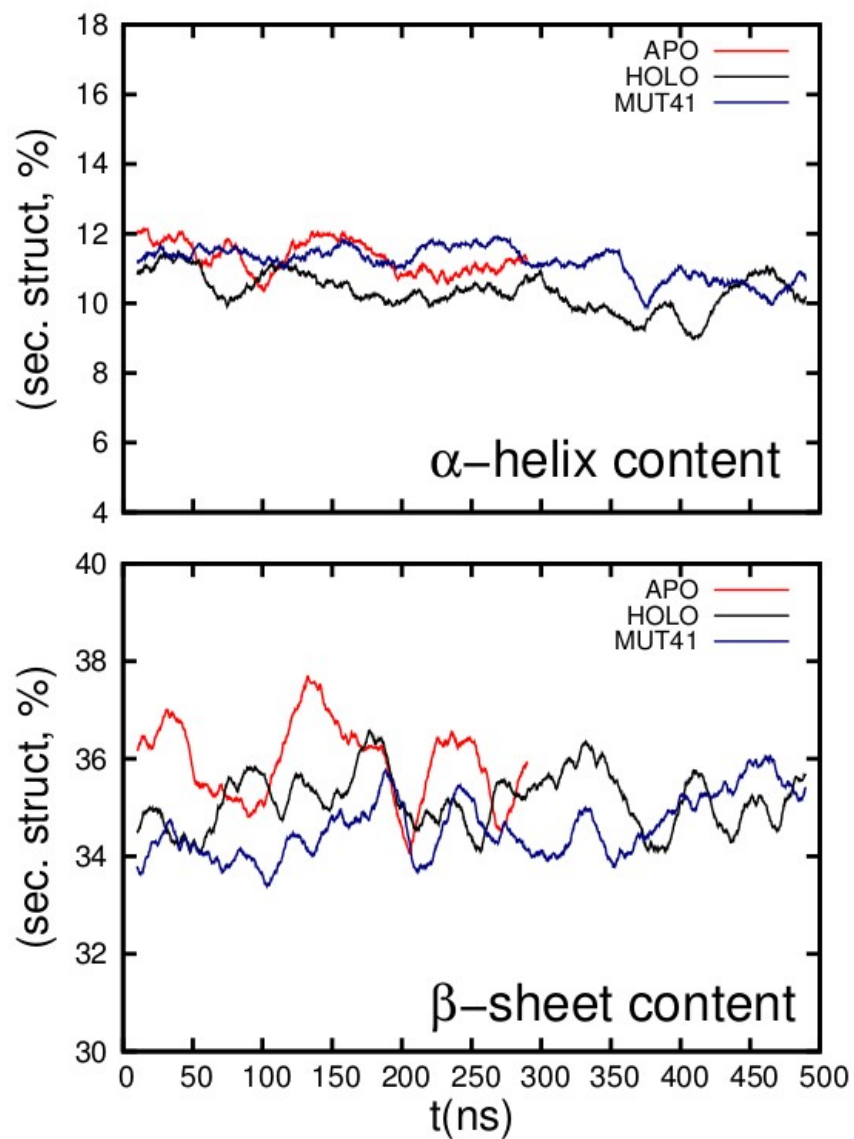


Figure S20 | Time evolution of the percentage of α -helix and β sheet content for the Apo (red), Wt (black) and K41C (blue). As in Fig S18, the Apo results go only until 300 ns as this simulation is shorter than the other two.

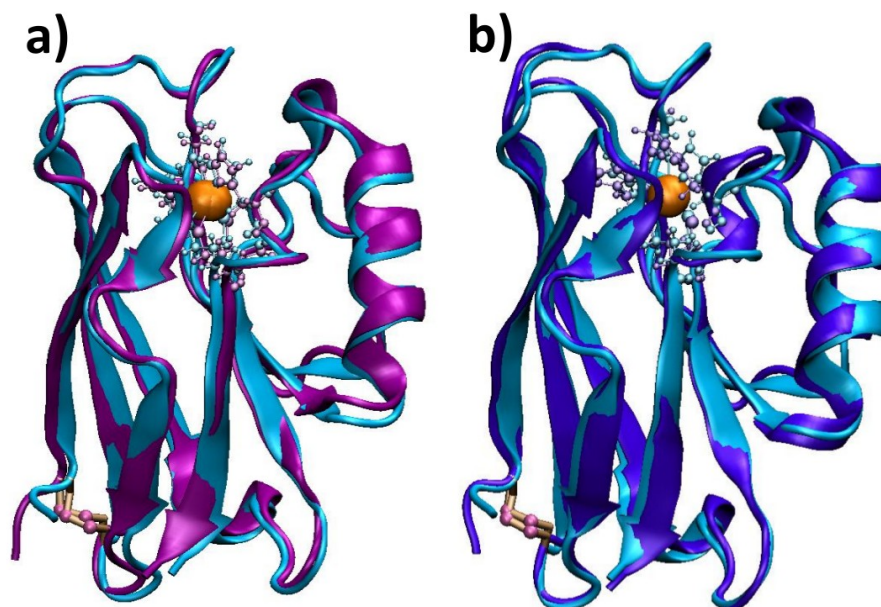


Figure S21 | Comparison between the final configurations obtained at the end of simulation of **(a)** the Wt (cyan) and K41C (magenta) structures; and **(b)** the Wt (cyan) and Apo (purple) structures. In both cases, the two structures compared have been aligned with the program Visual Molecular Dynamics. The copper atom is shown in its Van-der-Waals representation in an opaque orange color, and the disulfide bridge is shown in a bond representation colored in light orange.

-MD simulations of Wt-Azurin adsorption over Au(111):

In this section, we access how the structure of the Wt-Azurin is affected by its adsorption to a gold surface, and also which are the most likely adsorption orientations for the Azurin on Gold. Note, that here we have only considered the Wt, given the structural similarity between the three molecules considered in the previous section.

We initially position the Azurin along four different orientations on top of the gold surface. The reasoning for these orientations is the following. Let us consider the Azurin as a cylinder, where its axis passes through the center of the beta-sheet barrel. Then one can orient this barrel either as being standing vertically over the surface with the cysteines close to it (Fig S22 O2 initial) or with the cysteines the further away as possible from the surface (Fig S22 O4 initial). Also we can place this barrel flat on top of the surface with the cysteins in close contact with the surface (Fig S22 O1 initial), or with the cysteines the further away as possible from the surface (Fig S22 O3 initial). In all cases the initial distance between the protein and the surface is above 1nm, so we

give enough freedom for the protein to reorient itself if it must. Also it is important to notice that in all cases the system is fully embedded in water, which is not represented here for the sake of the simplicity of the representations. In all cases, once we have the protein oriented over the surface and the system solvated, then we leave the protein adsorb freely in a MD simulation that lasts 150ns, which we have found to be enough to reach a thermal equilibrium configuration.

In order to validate the previous orientation picture, we have performed two additional MD simulations concerning the adsorption of the K41C and Apo-Azurin over gold along the orientation O1. The results are presented in Fig. S23 and show that for the three cases (*i.e.* Wt-Holo, K41C and Wt-Apo), the final adsorption configuration is very similar, thus strengthening our hypothesis that this point mutation will not produce significant modifications in the final adsorption configuration and, therefore, it shall not alter the contact surface-protein-tip obtained for the Wt-Holo Azurin.

Looking to the evolution of the total energy for the 4 orientations (see Fig S24a)), it is clear that the Wt is stably absorbed to the surface after 100ns of simulation, given that the time evolution of the total energy seem to be stable beyond that time for all orientations. Moreover, the absorption energy seems to be very similar in all cases. Note that although we have shown in previous works that total energies allow us to get a good estimate for relative energies of adsorption for the different orientations³⁸, a proper assessment of this quantity would require free energy methods such as the one employed by Vilhena *et al.*³⁸. At last, concerning the adsorption process, we observed that in all cases the protein spontaneously absorbs over the gold surface, which is compatible with the fast sample preparation times seen in the experiments.

In Fig S22-23, the final configurations obtained at the end of the simulation for the four Azurin orientations are also showed. A close inspection of these figures allows us to conclude that the Cu-Azurin is absorbed to the gold surface via two different parts: the cysteines (O1 and O2), or the hydrophobic patch (O3 and O4). Note that in some cases, the protein needs a major reorienting so this occurs. One clear example of this is seen for orientation O3, where the protein rotates over ninety degrees so to adsorb via the hydrophobic patch. These two types of adsorptions are also evidenced by other observables. In fact, one realizes that the evolution of the RMSD of the protein (Fig. S24b)) and the beta sheet content (Fig. S25b)), clearly has two different trends. These two trends can be distinguished also in the evolution of the contact area (see Fig. S26a)): the O1 and O2 initial configurations are absorbed with larger contacts areas (more residues in contact with the surface, see footprints in Fig. S26b)), while de O3 and O4

orientations are less in contact with the surface, and use the hydrophobic patch as anchorage point.

In summary, we observed that upon adsorption to gold, Azurin seems to preserve most of its secondary structure (see Fig. S25b). Furthermore, starting from four very different adsorption configurations, we saw that the Azurin stably adsorbed along two different orientations. These results highlight that process of adsorption of the Copper-Azurin is guided via two well-defined sites: the hydrophobic patch and the naturally present cysteines.

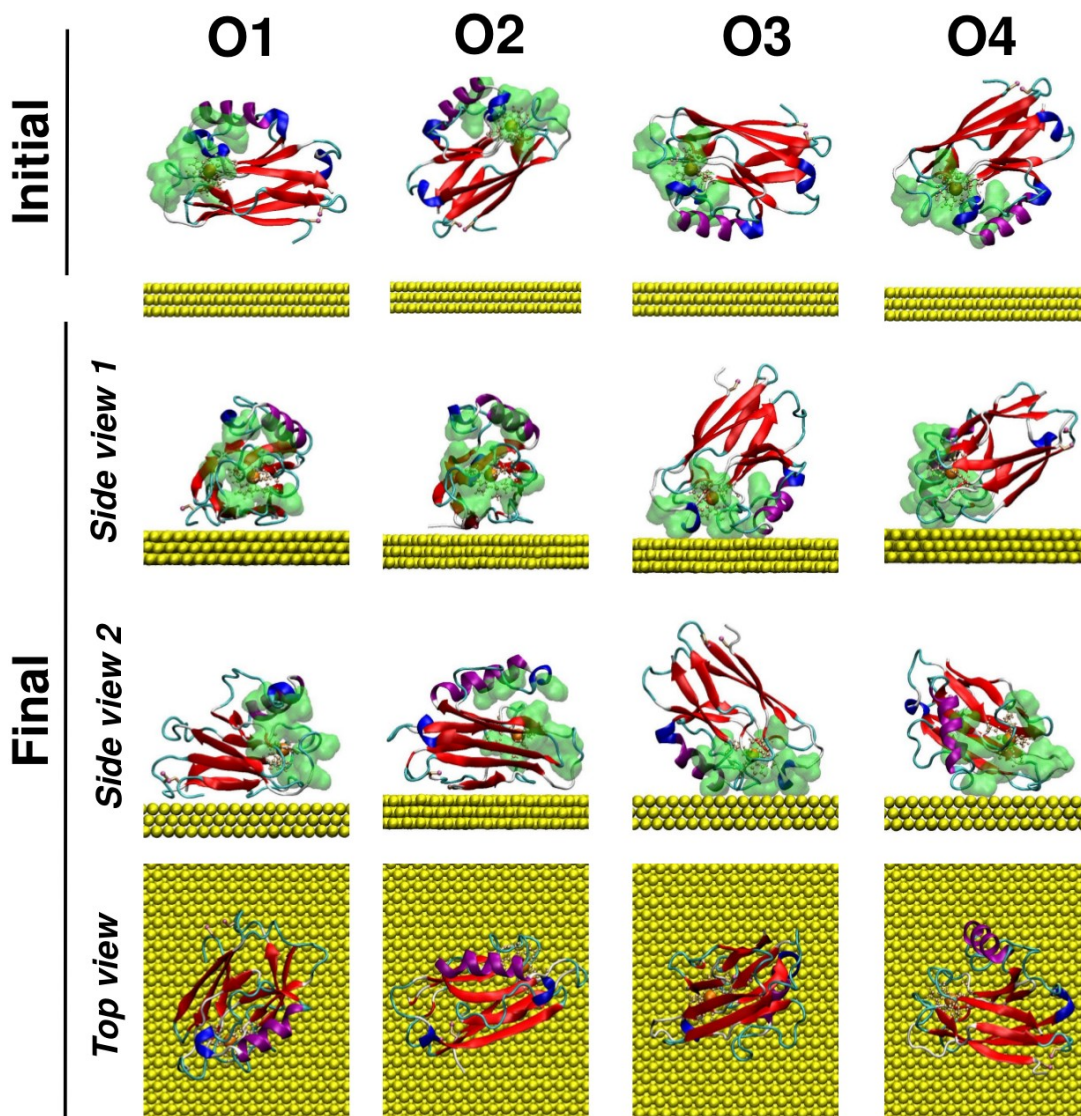


Figure S22 | Snapshots of the initial and final configurations of the Cu-Azurin adsorbed in a gold surface for the four different orientations studied (O1, O2, O3 and O4). From top to bottom, the first row corresponds to the initial configuration of the Azurin. In the second and third rows, two different side views of the final configurations obtained after 150 ns of simulation are showed. The fourth row corresponds to the top view of the Azurin absorbed in gold at the end of the simulation. The color representation used for the protein is the same as in Fig S17. Moreover, the position of the hydrophobic patch has been marked with a green Connolly surface³⁷.

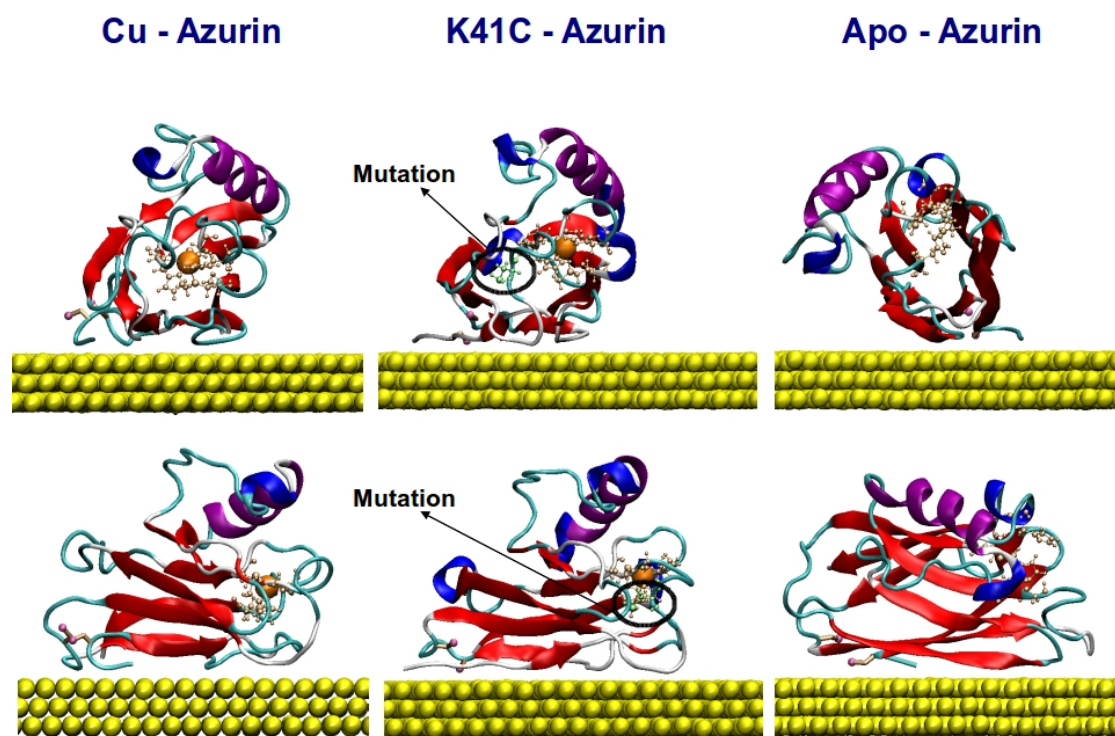


Figure S23 | Snapshots of the final configurations, (Side View1 on top and Side View2 on the bottom row) of the Cu-Azurin adsorbed in a gold surface for three different structures Wt-Holo, K41C and Wt-Apo Azurin. For the color code and representation scheme see Fig.S22.

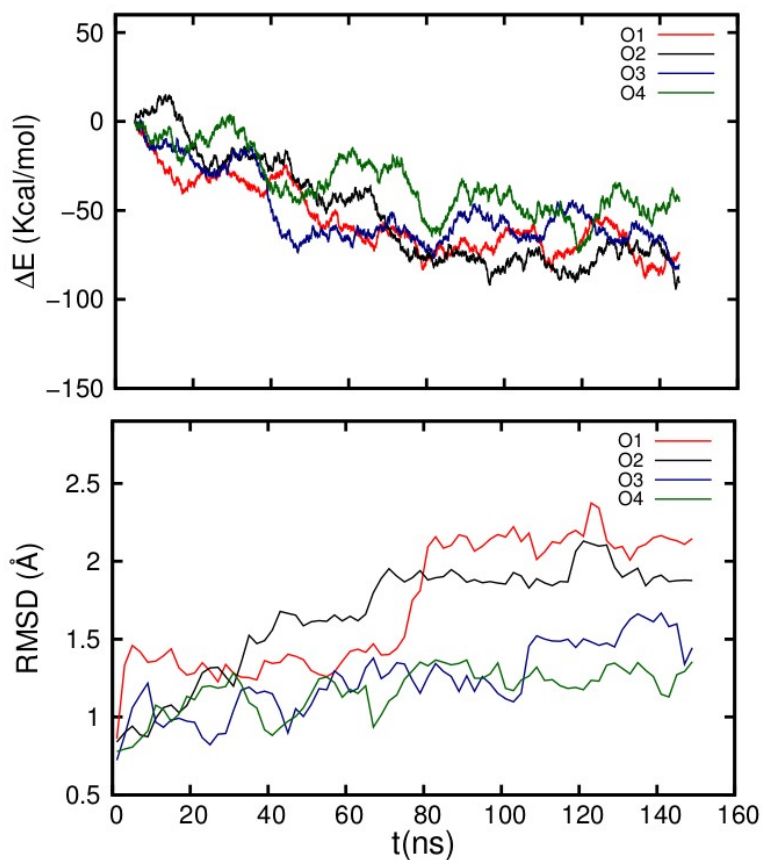


Figure S24 | Evolution of the total energy change (top) and the root-mean-square deviation, RMSD, (bottom) for the four different orientations analyzed (O1, O2, O3 and O4) during the absorption of the Cu-Azurin in gold. The average of the total energy in the first 10 ns has been taken as our energy reference. RMSD has been calculated for all the backbone atoms of the protein.

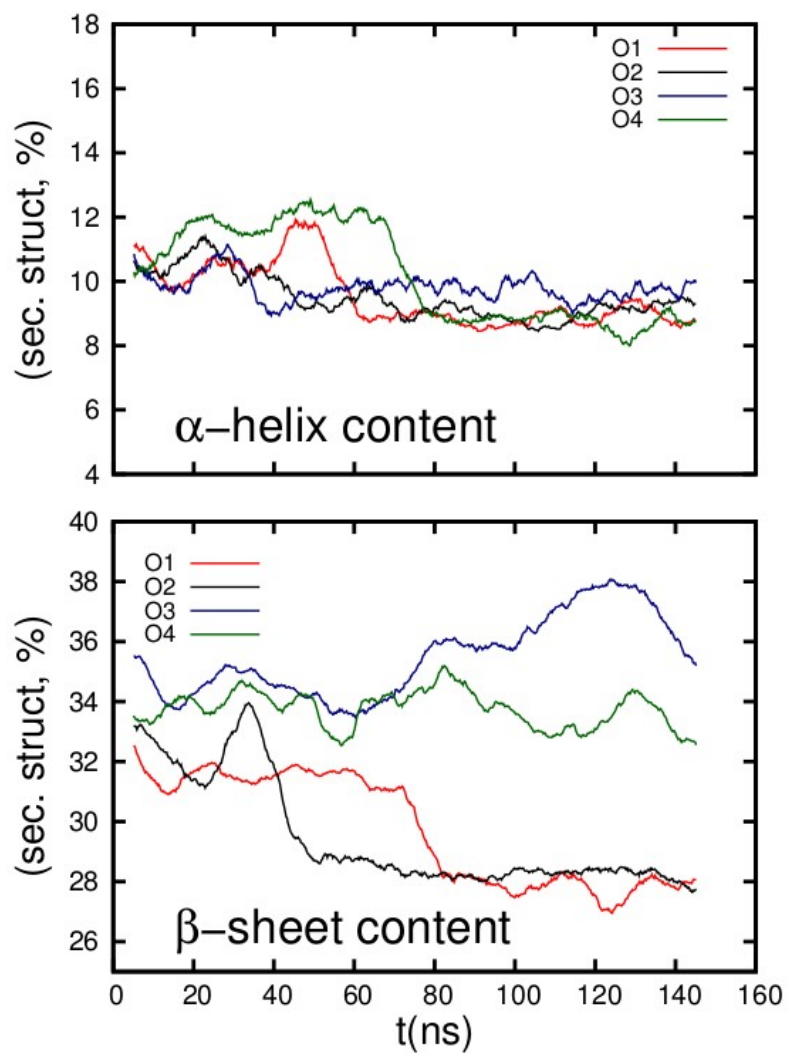


Figure S25 | Time evolution of the percentage of α -helix and β sheet content for the four different orientations (O1, O2, O3, and O4) analyzed of the Cu-Azurin adsorbed to gold

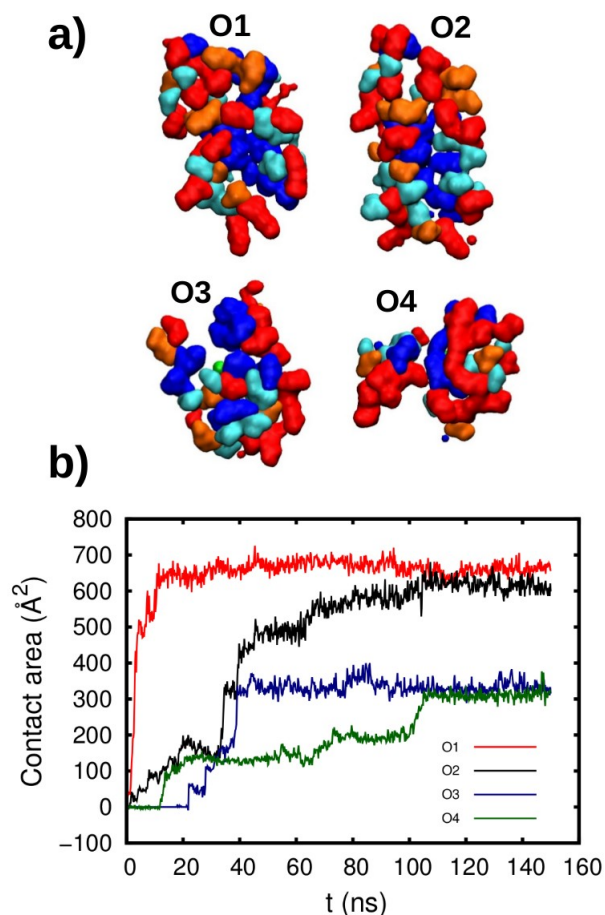


Figure S26 | (a) Residue distribution for the Cu-Azurin zone facing the gold surface in the final configuration for the four orientations analyzed (O1, O2, O3, and O4). The residues color is in accordance with their hydrophobicity index: very hydrophobic, hydrophobic, neutral, and hydrophilic residues are colored in blue, cyan, orange, and red, respectively. The copper atom is colored in green. (b) Time evolution of the contact surface area in Å² for the four orientations studied of the Cu-Azurin adsorbed in gold

-Influence of a gold tip on the structural stability of the Azurin as a function of the tip indentation height:

In this section, we access how the secondary structure of the Wt-Azurin is affected by the indentation of a gold tip. In these simulations, the tip moves towards the surface at a velocity of 0.2 nm/ns, while the protein adsorbed at the surface, is free to move and accommodate any deformation. In Fig S27, we show some snapshots of such process. From these snapshots one

observes that the secondary structure of the protein remains stable up to tip-surface distances of 2.3 nm. Beyond this indentation height, one observes that the Cu-Azurin starts to lose its secondary structure. This loss mostly occurs at the top alpha-helix. In contrast with this behavior we observe that the beta-barrel is able to sustain its secondary structure as we indent. In fact, during the indentation we observe how it goes from an almost cylindrical section barrel to a more ellipse alike. This additional degree of freedom allows this structure to better accommodate the deformation imposed by the tip. In fact, we observed that beta barrel seems to be stable even at tip-surface distances of 2 nm.

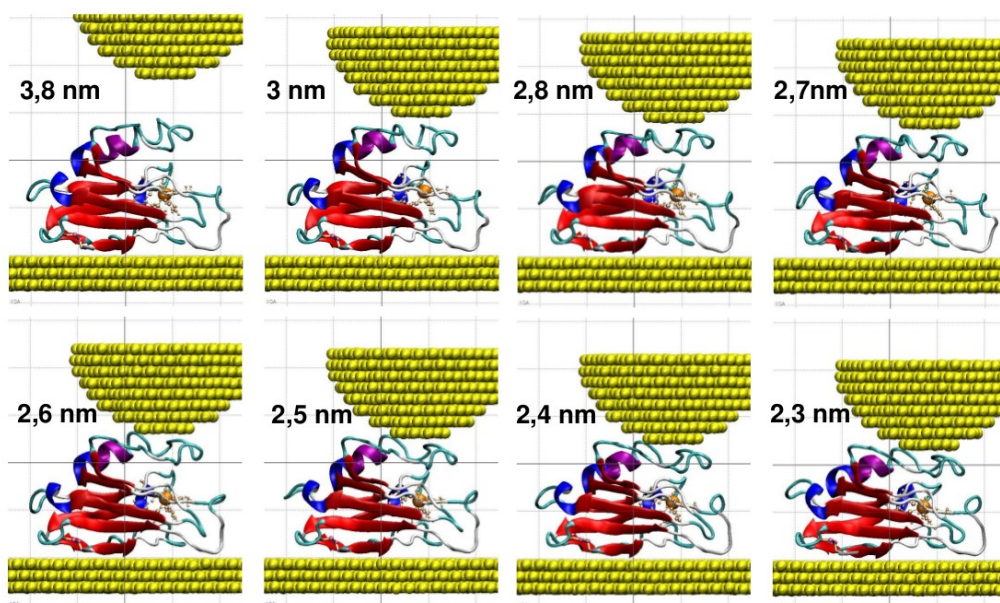


Figure S27 | Snapshots of the configuration of the Wt-Azurin being indented by a gold tip. Here we have considered tip-surface separations ranging from 4 nm to 2 nm. From left to right, and top to bottom, the distance between the tip and the gold surface has been reduced. The color representation used for the protein is the same as in Fig S17.

c) Temperature-dependent conductance in a sequential 2-step model

Figure S28 shows the conductance dependence on temperature for a sequential 2-step tunnelling mechanism described by the Equation (1) in the manuscript. Due to the sharp increase in conductance as the $\eta=0$ point is approached, the curves show the current-normalized first derivative at the different η . Note that when $\eta=0$, the conductance becomes poorly dependent on temperature, which is compatible with our results on the Wt protein.

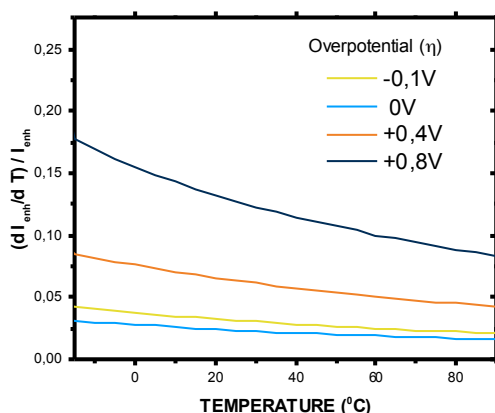


Figure S28 | Temperature-dependent enhanced current plots at different values of applied overpotential η for a sequential 2-step tunnelling model. The representation shows the first derivative normalized by the current at each point.

References

- (1) Guzzi, R.; La Rosa, C.; Grasso, D.; Milardi, D.; Sportelli, L. *Biophys. Chem.* **1996**, *60* (1), 29.
- (2) Huang, Q.; Quiñones, E. *Arch. Biochem. Biophys.* **2008**, *477* (1), 175.
- (3) Chi, Q.; Zhang, J.; Andersen, J. E. T.; Ulstrup, J. *J. Phys. Chem. B* **2001**, *105* (20), 4669.
- (4) Giannotti, M. I.; Cabeza de Vaca, I.; Artés, J. M.; Sanz, F.; Guallar, V.; Gorostiza, P. *J. Phys. Chem. B* **2015**, *119* (36), 12050.
- (5) Delfino, I.; Cannistraro, S. *Biophys. Chem.* **2009**, *139* (1), 1.
- (6) Frisch, M. J.; Trucks, G. W.; Schlegel, H. B.; Scuseria, G. E.; Robb, M. A.; Cheeseman, J. R.; Scalmani, G.; Barone, V.; Mennucci, B.; Petersson, G. A.; Nakatsuji, H.; Caricato, M.; Li, X.; Hratchian, H. P.; Izmaylov, A. F.; Bloino, J.; Zheng, G.; Sonnenberg, J. L.; Hada, M.; Ehara, M.; Toyota, K.; Fukuda, R.; Hasegawa, J.; Ishida, M.; Nakajima, T.; Honda, Y.; Kitao, O.; Nakai, H.; Vreven, T.; Montgomery Jr., J. A.; Peralta, J. E.; Ogliaro, F.; Bearpark, M.; Heyd, J. J.; Brothers, E.; Kudin, K. N.; Staroverov, V. N.; Kobayashi, R.; Normand, J.; Raghavachari, K.; Rendell, A.; Burant, J. C.; Iyengar, S. S.; Tomasi, J.; Cossi, M.; Rega, N.; Millam, J. M.; Klene, M.; Knox, J. E.; Cross, J. B.; Bakken, V.; Adamo, C.; Jaramillo, J.; Gomperts, R.; Stratmann, R. E.; Yazyev, O.; Austin, A. J.; Cammi, R.; Pomelli, C.; Ochterski, J. W.; Martin, R. L.; Morokuma, K.; Zakrzewski, V. G.; Voth, G. A.; Salvador, P.; Dannenberg, J. J.; Dapprich, S.; Daniels, A. D.; Farkas, Ö.; Foresman, J. B.; Ortiz, J. V.; Cioslowski, J.; Fox, D. J. *Gaussian Inc Wallingford CT*. Gaussian, Inc. 2009, p Wallingford CT.
- (7) Yanai, T.; Tew, D. P.; Handy, N. C. *Chem. Phys. Lett.* **2004**, *393* (1–3), 51.
- (8) Peach, M. J. G.; Helgaker, T.; Sałek, P.; Keal, T. W.; Lutnaes, O. B.; Tozer, D. J.; Handy, N. C. *Phys. Chem. Chem. Phys.* **2006**, *8* (5), 558.
- (9) Reimers, J. R.; Cai, Z.-L.; Bilić, A.; Hush, N. S. *Ann. N. Y. Acad. Sci.* **2003**, *1006* (1), 235.

- (10) Reimers, J. R.; Solomon, G. C.; Gagliardi, A.; Bilić, A.; Hush, N. S.; Frauenheim, T.; Di Carlo, A.; Pecchia, A. *J. Phys. Chem. A* **2007**, *111* (26), 5692.
- (11) Cai, Z. L.; Crossley, M. J.; Reimers, J. R.; Kobayashi, R.; Amos, R. D. *J. Phys. Chem. B* **2006**, *110* (31), 15624.
- (12) Blanco-Rodríguez, A. M.; Di Bilio, A. J.; Shih, C.; Museth, A. K.; Clark, I. P.; Towrie, M.; Cannizzo, A.; Sudhamsu, J.; Crane, B. R.; Sýkora, J.; Winkler, J. R.; Gray, H. B.; Záliš, S.; Vlček, A. *Chem. - A Eur. J.* **2011**, *17* (19), 5350.
- (13) Dreuw, A.; Head-Gordon, M. *Chemical Reviews*. American Chemical Society November 2005, pp 4009–4037.
- (14) Jensen, L.; Govind, N. *The journal of physical chemistry. A*. American Chemical Society September 2009, pp 9761–9765.
- (15) Orian, L.; Carlotto, S.; Di Valentin, M.; Polimeno, A. *J. Phys. Chem. A* **2012**, *116* (15), 3926.
- (16) Polander, L. E.; Tiwari, S. P.; Pandey, L.; Seifried, B. M.; Zhang, Q.; Barlow, S.; Risko, C.; Brédas, J. L.; Kippelen, B.; Marder, S. R. *Chem. Mater.* **2011**, *23* (15), 3408.
- (17) Hanwell, M. D.; Curtis, D. E.; Lonie, D. C.; Vandermeersch, T.; Zurek, E.; Hutchison, G. R. *J. Cheminform.* **2012**, *4* (8), 17.
- (18) <http://ambermd.org/> **2014**.
- (19) Salomon-Ferrer, R.; Götz, A. W.; Poole, D.; Le Grand, S.; Walker, R. C. *J. Chem. Theory Comput.* **2013**, *9* (9), 3878.
- (20) Götz, A. W.; Williamson, M. J.; Xu, D.; Poole, D.; Le Grand, S.; Walker, R. C. *J. Chem. Theory Comput.* **2012**, *8* (5), 1542.
- (21) Le Grand, S.; Götz, A. W.; Walker, R. C. *Comput. Phys. Commun.* **2013**, *184* (2), 374.
- (22) Pérez, A.; Marchán, I.; Svozil, D.; Sponer, J.; Cheatham, T. E.; Loughton, C. A.; Orozco, M. *Biophys. J.* **2007**, *92* (11), 3817.
- (23) Cornell, W. D.; Cieplak, P.; Bayly, C. I.; Gould, I. R.; Merz, K. M.; Ferguson, D. M.; Spellmeyer, D. C.; Fox, T.; Caldwell, J. W.; Kollman, P. A. *J. Am. Chem. Soc.* **1995**, *117* (19), 5179.
- (24) van den Bosch, M.; Swart, M.; Snijders†, J. G.; Berendsen, H. J. C.; Mark, A. E.; Oostenbrink, C.; van Gunsteren, W. F.; Canters, G. W. *ChemBioChem* **2005**, *6* (4), 738.
- (25) Paltrinieri, L.; Borsari, M.; Ranieri, A.; Battistuzzi, G.; Corni, S.; Bortolotti, C. A. *J. Phys. Chem. Lett.* **2013**, *4* (5), 710.
- (26) Beedle, A. E. M.; Lezamiz, A.; Stirnemann, G.; Garcia-Manyes, S. *Nat. Commun.* **2015**, *6*.
- (27) Zanetti-Polzi, L.; Bortolotti, C. A.; Daidone, I.; Aschi, M.; Amadei, A.; Corni, S. *Org. Biomol. Chem.* **2015**, *13* (45), 11003.
- (28) Zanetti-Polzi, L.; Corni, S.; Daidone, I.; Amadei, A. *Phys. Chem. Chem. Phys.* **2016**, *18* (27), 18450.

- (29) Jorgensen, W. L.; Chandrasekhar, J.; Madura, J. D.; Impey, R. W.; Klein, M. L. *J. Chem. Phys.* **1983**, *79* (2), 926.
- (30) Joung, I. S.; Cheatham, T. E. *J. Phys. Chem. B* **2009**, *113* (40), 13279.
- (31) Li, P.; Roberts, B. P.; Chakravorty, D. K.; Merz, K. M. *J. Chem. Theory Comput.* **2013**, *9* (6), 2733.
- (32) Heinz, H.; Lin, T.-J.; Kishore Mishra, R.; Emami, F. S. *Langmuir* **2013**, *29* (6), 1754.
- (33) Heinz, H.; Ramezani-Dakhel, H. *Chem. Soc. Rev.* **2016**, *45* (2), 412.
- (34) Berman, H. M.; Westbrook, J.; Feng, Z.; Gilliland, G.; Bhat, T. N.; Weissig, H.; Shindyalov, I. N.; Bourne, P. E. *Nucleic Acids Res.* **2000**, *28* (1), 235.
- (35) Nar, H.; Messerschmidt, A.; Huber, R.; van de Kamp, M.; Canters, G. W. *J. Mol. Biol.* **1991**, *221* (3), 765.
- (36) Gordon, J. C.; Myers, J. B.; Folta, T.; Shoja, V.; Heath, L. S.; Onufriev, A. *Nucleic Acids Res.* **2005**, *33* (Web Server), W368.
- (37) Connolly, M. L.; IUCr. *J. Appl. Crystallogr.* **1983**, *16* (5), 548.
- (38) Vilhena, J. G.; Rubio-Pereda, P.; Velloso, P.; Serena, P. A.; Pérez, R. *Langmuir* **2016**, *32* (7), 1742.